

Process-based hierarchical models for coupling high-dimensional LiDAR and forest variables over large geographic domains

Andrew O. Finley, Sudipto Banerjee, Yuzhen Zhou, and Bruce D. Cook*

Abstract

Recent advancements in remote sensing technology, specifically Light Detection and Ranging (LiDAR) sensors, provide the data needed to quantify forest characteristics at a fine spatial resolution over large geographic domains. From an inferential standpoint, there is interest in prediction and interpolation of the often spatially misaligned LiDAR signals and forest variables. We propose a fully process-based Bayesian hierarchical model for above ground biomass (AGB) and LiDAR signals. The process-based framework offers richness in inferential capabilities (e.g., inference on the entire underlying processes instead of their values only at pre-specified points) and their easier interpretability. Key challenges we obviate include misalignment between the AGB observations and LiDAR signals and the high-dimensionality in the model emerging from LiDAR signals in conjunction with the large number of spatial locations. We offer simulation experiments to evaluate our proposed models and also apply them to a challenging dataset comprising LiDAR and spatially coinciding forest inventory variables collected on the Penobscot Experimental Forest (PEF), Maine. Our key substantive contributions include AGB data products with associated measure of uncertainty for the PEF and, more broadly, a methodology that should find use in a variety of current and upcoming forest variable mapping efforts using remotely sensed high-dimensional data.

*Andrew O. Finley (e-mail: finleya@msu.edu), Department of Forestry, Michigan State University; Sudipto Banerjee, Department of Biostatistics, University of California Los Angeles; Yuzhen Zhou, Department of Statistics, University of Nebraska-Lincoln; Bruce D. Cook, Biospheric Sciences Laboratory, NASA Goddard Space Flight Center.

1 Introduction

Linking forest inventory with air- and space-borne Light Detection and Ranging (LiDAR) datasets via regression models offers an attractive approach to mapping forest variables at stand, regional, continental, and global scales. Because of its ability to characterize vertical and horizontal forest structure, LiDAR data have shown great potential for use in estimating spatially explicit forest variables over a range of geographic scales (Asner et al. 2009; Babcock et al. 2013; Finley et al. 2011; Iqbal et al. 2013; Muss et al. 2011; Næsset 2011; Neigh et al. 2013). Encouraging results from these and many other studies have spurred massive investment in new LiDAR sensors, sensor platforms, as well as extensive campaigns to collect field-based calibration data. For example, ICESat-2—planned for launch in 2017—will be equipped with a LiDAR sensor able to gather data from space at unprecedented spatial resolutions (Abdalati et al. 2010). As currently proposed, ICESat-2 will be a photon-counting sensor capable of recording measurements on a \approx 70 cm footprint (ICESat-2 2015). The Global Ecosystem Dynamics Investigation LiDAR (GEDI) will be an International Space Station mounted system capable of producing 25 m diameter footprint waveforms and is scheduled to be operational in 2018 (GEDI 2014). One of GEDI’s core objectives is to quantify the distribution of above ground biomass (AGB) at a fine spatial resolution. NASA Goddard’s LiDAR, Hyper-spectral, and Thermal (G-LiHT) imager is an air-borne platform developed, in part, to examine how future space-originating LiDAR, e.g., ICESat-2, GEDI, or other platforms, may be combined with field-based validation measurements to build predictive models for AGB and other forest variables (Awadallah et al. 2013; Cook et al. 2013).

Along with increasing attention given to development of LiDAR data acquisition systems, there is continued and expanding interest in acquiring long-term forest inventory datasets for ecosystem monitoring initiatives (Albercht et al. 2012; Phillips et al. 1998; Talbot et al. 2014). Long-term forest inventories including the United States Forest Service’s Forest Inventory and Analysis (FIA) program, Long-Term Ecological Research Network (LTER), and National

Ecological Observatory Network (NEON) are collecting massive amounts of space and time indexed ecological data (Kampe et al. 2010; Michener et al. 2011; Smith 2002). These datasets provide the calibration measurements necessary for large-scale mapping of forest variables using LiDAR data (Healey et al. 2012).

Much of the interest in LiDAR based forest variable mapping is to support carbon monitoring, reporting, and verification (MRV) systems, such as defined by the United Nations Programme on Reducing Emissions from Deforestation and Forest Degradation (UN-REDD) and NASA's Carbon Monitoring System (CMS) (Le Toan et al. 2011; Ometto et al. 2014; UN-REDD 2009; CMS 2010). In these, and similar initiatives, AGB is the forest variable of interest because it provides a nearly direct measure of forest carbon (i.e., carbon comprises $\sim 50\%$ of wood biomass, West 2004). Most efforts to quantify and/or manage forest ecosystem services, e.g., carbon, biodiversity, water, seek high spatial resolution data products such as gridded maps with associated measures of uncertainty, e.g., point and associated credible intervals (CIs) at the pixel level. In fact several high profile international initiatives include language concerning the level of spatially explicit acceptable error in total forest carbon estimates, see, e.g., UN-REDD (2009) and UNFCCC (2015).

Many current LiDAR data acquisition campaigns focus on achieving complete coverage at a high spatial resolution over the domain of interest, e.g., resulting in a fine grid with each pixel yielding a high-dimensional LiDAR signal. In practice, a variety of non-statistical approaches are then used to characterize the LiDAR signals—effectively a dimension reduction step, Anderson et al. (2008), Gonzalez et al. (2010), Muss et al. (2011), Tonolli et al. (2011), Popescu and Zhao (2008), and Babcock et al. (2013). These signal characteristics serve as regressors in models where the outcome forest variables are measured at a relatively small set of georeferenced forest inventory plots. The regression model is then used to predict the forest outcome variables at all LiDAR pixels across the domain. This approach works well for small-scale forest variable mapping efforts. However, next generation LiDAR acquisition campaigns, such as ICESat-2, GEDI, and G-LiHT (see, e.g., Stockton 2014), aimed at

mapping and quantifying forest variables over large spatial extents will collect LiDAR data samples from the domain of interest, e.g., using transect or cluster designs. The designs specify point-referenced LiDAR sampling across the domain extent and also over forest inventory plot locations (again for regression model calibration). In such settings the primary objective is still delivery of high resolution (complete-coverage) spatial predictive maps of forest variables, but also corresponding maps of LiDAR signal predictions at non-sampled locations. Further, to inform future LiDAR collection sampling designs, there is interest in characterizing the spatial dependence of within and, more importantly, among LiDAR signals. This information can help guide LiDAR sampling strategies with the aim to maximize some information gain criterion; see, e.g., Xia et al. (2006), Mateu and Müller (2012).

We propose a flexible framework to jointly model spatially misaligned LiDAR signals and forest inventory plot outcomes (e.g., AGB) that will *i*) extract information from the high-dimensional LiDAR signals to explain variability in the forest variable of interest, *ii*) estimate spatial dependence among and within LiDAR signals to improve inference and possibly help inform future LiDAR sampling strategies, and *iii*) provide full posterior predictive inference for both LiDAR signals and forest variables at locations where either one or neither of the data sources are available.

Meeting these objectives is particularly challenging for several reasons. From a computational standpoint each LiDAR signal is high-dimensional and the signals as well as the forest inventory plots are observed at a potentially large number of locations. From a model specification standpoint there are several sources of dependence that should be accommodated, including *i*) within and between LiDAR signals, *ii*) between LiDAR signals and spatially proximate forest variable measurements, and *iii*) residual spatial dependence in the signals and forest variables. These dependencies often result from strong vertical and horizontal similarities in forest structure caused by past management and/or natural disturbances.

Our primary methodological contribution is the development of a modeling framework for high-dimensional misaligned data. Given the rich inference we seek (see preceding para-

graph), our Bayesian hierarchical models jointly model LiDAR signals and forest variables as a random process using latent Gaussian processes (GPs). This considerably enhances the computational burden of fitting them to datasets with a large number of spatial locations. The costs are exacerbated further by even a modest number of heights at which the LiDAR signal is observed. We achieve dimension reduction through bias-adjusted reduced-rank representations for the joint LiDAR-AGB process.

The manuscript is organized as follows. Section 2 provides an overview of the motivating dataset that comprises G-LiHT LiDAR and AGB measured at forest inventory plots on the Penobscot Experimental Forest (PEF) in Bradley, Maine. Section 3 describes the proposed hierarchical model along with details on Bayesian estimation, prediction, and implementation. Section 5 offers an analysis of a synthetic dataset and PEF analysis. Finally, Section 6 concludes the manuscript with a brief summary and pointers toward future work.

2 Data

The PEF is a 1600 ha tract of Acadian forest located in Bradley, Maine ($44^{\circ} 52' N$, $68^{\circ} 38' W$). The forest is divided into over 50 management units (MU)—delineated as black polygons in Figure 1(a)—that received management and monitoring since the 1950s (Sendak et al. 2003). Within each MU, different silvicultural treatments are implemented, e.g., unregulated harvest, shelterwood, diameter limit cutting, or natural regeneration. Following procedures described in Finley et al. (2014), AGB (Mg/ha) was calculated for each of 451 permanent sample plots (PSPs) across the PEF, shown as point symbols in Figure 1(a). The underlying surface in Figure 1(a) was generated by passing the point-referenced AGB through a non-statistical interpolator. Due to MU specific harvesting and subsequent regrowth cycles, the surface exhibits patterns of spatial dependence with relatively strong homogeneity within MUs. For example, MU U7B—highlighted in Figure 1(a)—received a shelterwood harvest in 1978 with a final overstory harvest in 2003. This silvicultural treatment results in a MU with relatively young trees and even-aged composition with low AGB (indicated by a lighter surface color in Figure 1(a)). In contrast to U7B, C12 is characterized by older and larger

trees, but also greater vertical and horizontal forest structure complexity due to repeated selection harvests that aim to concentrate growth on economically desirable trees. Sendak et al. (2003) and Hayashi et al. (2014) provide additional silvicultural treatment details.

Large footprint waveforms, characteristic of space-based LiDAR sensors, were calculated using discrete multistop returns from a 2013 PEF G-LiHT data acquisition campaign (Cook et al. 2013). As noted in Section 1, G-LiHT is a portable multi-sensor airborne system developed by NASA Goddard Space Flight Center that simultaneously maps the composition and structure of terrestrial ecosystems. The G-LiHT laser scanner (VQ-480, Riegl Laser Measurement Systems, Horn, Austria) uses a 1550 nm laser that provides an effective measurement rate of up to 150 kHz along a 60° swath perpendicular to the flight direction. At a nominal flying altitude of 335 m, each laser pulse has a footprint approximately 10 cm in diameter and is capable of producing up to 8 returns. Following data processing methods in Blair and Hofton (1999), G-LiHT produced 26,286 georeferenced pseudo-waveform LiDAR signals across the PEF with 451 of these spatially coinciding with the observed PSPs. Each pseudo-waveform covers a 15 m diameter footprint with a signal comprising 113 values between 0 and 33.9 m above the ground. A signal value is the amount of energy returned to the sensor from a given height divided by the total energy emitted by the sensor over the footprint (additional details are given in Section 5.2.1). The signal characterizes the vertical distribution of forest structure within the footprint. Signals corresponding to PSPs within the MUs highlighted in Figure 1(a) are shown in Figure 1(b). Here, U7B’s even-aged and structurally homogeneous composition is apparent in the signals’ consistent peak at ~8 m—corresponding to the densest layer of the forest canopy—and minimal energy returns above ~17 m—corresponding to maximum forest canopy height. In contrast, C12’s signals are characterized by non-zero values at greater heights—reflecting the prevalence of taller trees—and greater vertical distribution of energy returns—indicative of a vertically complex forest structure resulting from the MU’s silvicultural treatments.

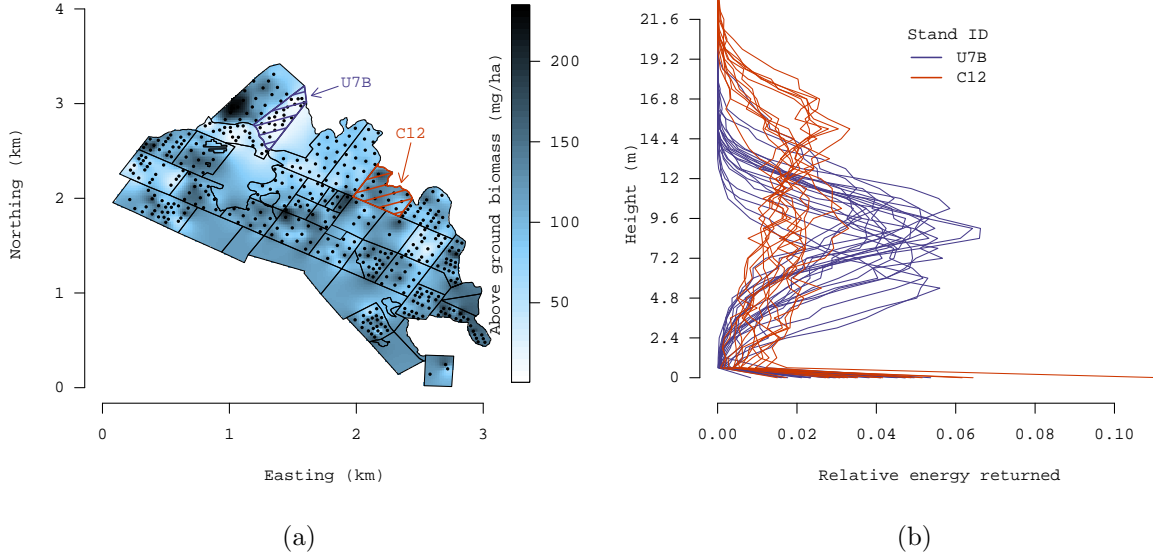


Figure 1: (a) Penobscot Experimental Forest, Maine, with management units and forest inventory plot locations delineated as polygons and points, respectively. (b) G-LiHT LiDAR signals observed at forest inventory plots highlighted in (a).

3 Models

We envision AGB as a continuous spatial process $\{y(\mathbf{s}) : \mathbf{s} \in \mathcal{D} \subset \mathbb{R}^2\}$ measured over a finite collection of PSP's $\mathcal{S} = \{\mathbf{s}_1, \mathbf{s}_2, \dots, \mathbf{s}_{n_s}\} \subset \mathcal{D}$. LiDAR signals are also assumed to arise as the partial realizations of a process $\{z(\ell) : \ell \in \mathcal{D} \times \mathcal{H}\}$, where $\ell = (\mathbf{s}, x)$ is a space-height coordinate, $z(\ell)$ represents the LiDAR signal's relative energy return at spatial location \mathbf{s} and height x , and \mathcal{H} is the compact interval $[0, M]$ representing the range of possible heights. The LiDAR signals are also measured at the PSP's in \mathcal{S} and heights $\mathcal{X} = \{x_1, x_2, \dots, x_{n_x}\} \subset \mathcal{H}$. We will assume that $\mathcal{L} = \{\ell_1, \ell_2, \dots, \ell_n\}$ is a complete enumeration of space-height coordinates at which the LiDAR signals have been measured. Each ℓ_i will correspond to a unique ordered pair (\mathbf{s}_j, x_k) , where $\mathbf{s}_j \in \mathcal{S}$ and $x_k \in \mathcal{X}$. If the measurements are balanced across space and height, i.e., every PSP has measured the LiDAR signal at each of the points in \mathcal{X} , then there will be $n = n_s n_x$ measurements. This, however, need not be assumed for the subsequent development.

3.1 Model for $z(\ell)$

We write the LiDAR signal as

$$z(\ell) = \mu_z(\ell; \boldsymbol{\beta}_z) + u(\ell) + \epsilon_z(\ell) , \quad (1)$$

where $\mu_z(\ell; \boldsymbol{\beta}_z)$ is a mean function capturing large-scale variation, $u(\ell)$ is an underlying zero-centered stochastic process over $\mathcal{D} \times \mathcal{H}$, and $\epsilon_z(\ell) \stackrel{ind}{\sim} N(0, \tau_z^2(x))$ models random disturbances at finer scales, at least part of which is attributed to measurement error. The variance of this fine scale disturbance is assumed to remain invariant over the locations, but depends upon the height x at which the signal is measured.

We assume that $u(\ell)$ is a zero-centered Gaussian process over $\mathcal{D} \times \mathcal{H}$ with a covariance function $C_u(\ell, \ell'; \boldsymbol{\theta}_u) := \text{Cov}[u(\ell), u(\ell')]$. This function must ensure that the resulting variance-covariance matrix corresponding to realizations of the process over *any* finite subset of $\mathcal{D} \times \mathcal{H}$ is positive definite. A natural class of such functions is that of spatiotemporal covariance functions, but with the temporal domain being replaced by the “height” domain; Gneiting et al. (2006) and Gneiting and Guttorp (2010) provide excellent expositions.

A relevant concern in our current application is the lack of *separability*, i.e., the covariance function should not factorize into a purely spatial component and a purely “height” component. Separability would imply that the spatial association in the LiDAR signals remains invariant across heights and, similarly, the association among signals at different heights remains the same for each spatial location. This assumption is too stringent for our application; see, e.g., the disparity in empirical semivariogram parameter estimates presented in the supplemental web material. Furthermore, separable covariance functions violate the so called “screening” effect (Stein 2005) and the resulting associations can be sensitive to small perturbations in spatial locations.

Based upon the above, we use a slightly simpler version of a highly flexible class of

covariance functions developed by Gneiting (2002),

$$C_u(\ell, \ell'; \boldsymbol{\theta}_u) := \frac{\sigma_u^2}{(a|x - x'|^2 + 1)^\gamma} \exp\left(-\frac{c \|\mathbf{s} - \mathbf{s}'\|}{(a|x - x'|^2 + 1)^{\gamma/2}}\right), \quad (2)$$

where $\ell = (\mathbf{s}, x)$ and $\ell' = (\mathbf{s}', x')$, $\boldsymbol{\theta}_u = \{\sigma_u^2, a, \gamma, c\}$, $\sigma_u^2, a, c > 0$ and $\gamma \in [0, 1]$. Observe that the above covariance function still assumes isotropy, i.e., the associations depend upon the distances between the spatial locations and the absolute difference between the heights. This, too, is unlikely in practice, but we are less concerned here because nonstationarity will be introduced in the covariance structures as a part of dimension reduction (Section 3.3).

3.2 Model for $y(\mathbf{s})$ and $z(\ell)$

The spatial process for AGB, $y(\mathbf{s})$, shares the same spatial domain as the LiDAR process and can be modeled using a Gaussian process over \mathcal{D} . Thus,

$$y(\mathbf{s}) = \mu_y(\mathbf{s}; \boldsymbol{\beta}_y) + w(\mathbf{s}) + \epsilon_y(\mathbf{s}), \quad (3)$$

where $\mu_y(\mathbf{s}; \boldsymbol{\beta}_y)$ captures large scale variation or trends in AGB, $w(\mathbf{s})$ is a zero-centered spatial process, and $\epsilon_y(\mathbf{s})$ is a white noise process with zero mean and variance τ_y^2 to capture measurement error in AGB.

We posit that the process for AGB is associated with the process for the LiDAR signals and desire to estimate this association. One possibility is to treat $w(\mathbf{s})$ as a shared process between AGB and LiDAR and introduce it as an additive component in (1). This, however, causes identifiability issues. First, an additional additive process in (1) may be difficult to identify from $u(\ell)$ using a single partial realization of the LiDAR process. Second, the AGB process is then governed by a single shared process, $w(\mathbf{s})$, and adding a second process, say $v(\mathbf{s})$, to capture departure from the shared component will, again, introduce identifiability problems. Both these problems can, in principle, be resolved in Bayesian settings if prior elicitation was possible on these different component processes. This, unfortunately, is difficult here and we do not pursue such approaches here.

We prefer to treat $u(\ell)$ as a shared underlying process, common to both $z(\mathbf{s}; x)$ and $y(\mathbf{s})$. However, since the AGB has support over the spatial domain only, we assume that it is a continuous weighted average of $u(\ell)$ over \mathcal{X} . Therefore, we write $w(\mathbf{s})$ in (3) as

$$w(\mathbf{s}) = \int_{\mathcal{X}} \alpha(x) u(\mathbf{s}, x) dx + v(\mathbf{s}) \approx \sum_{j=1}^{n_x} \alpha(x_j) u(\mathbf{s}, x_j) + v(\mathbf{s}) , \quad (4)$$

where $\alpha(x)$ is a weight function that maps height in \mathcal{X} to the real line and $v(\mathbf{s})$ is a zero-centered spatial process, independent of $u(\mathbf{s}, x)$, that captures features specific to AGB that are not shared with the LiDAR signal. Specifically, we assume $v(\mathbf{s})$ is a zero-mean Gaussian process with an exponential covariance function $C_v(\mathbf{s}, \mathbf{s}'; \boldsymbol{\theta}_v) = \sigma_v^2 \exp(-\phi_v \|\mathbf{s} - \mathbf{s}'\|)$, where $\boldsymbol{\theta}_v = \{\sigma_v^2, \phi_v\}$. This choice ensures that the process realizations are not overly smooth—they are mean-square continuous but not differentiable—and compensates for the possible oversmoothing by the averaging of the shared process. More generally, a Matérn covariance function with a prior on the smoothness parameter could have been used, but this does adds to the computational burden without any discernible benefits in the substantive scientific inference we seek in the current application.

Rather than specify the weights $\alpha(x)$, we represent the integrated process in (4) as a linear combination of the $u(\ell)$'s over \mathcal{X} for any fixed \mathbf{s} and regard the $\alpha(x_j)$'s as unknown coefficients for the $u(\mathbf{s}, x_j)$'s. These coefficients capture the dependence of $w(\mathbf{s})$ on $u(\ell)$ and, hence, the association between the two processes. If they are all estimated to be effectively zero, then the data does not reflect associations between the AGB and LiDAR processes, while significant departures of any of the coefficients from zero will indicate association between the processes.

Let \mathbf{u} be the $n \times 1$ vector with elements $u(\ell_i)$, $i = 1, 2, \dots, n$ stacked so that $\ell_i = (\mathbf{s}_j, x_k)$, where $i = (j-1)n_x + k$ with $j = 1, 2, \dots, n_s$ and $k \in \{1, 2, \dots, n_x\}$, and $\mathbf{C}_u(\boldsymbol{\theta}_u)$ is the corresponding $n \times n$ variance-covariance matrix with entries $\text{cov}[u(\ell_i), u(\ell_j)]$. For the spatial process $v(\mathbf{s})$, we let \mathbf{v} be the $n_s \times 1$ vector with elements $v(\mathbf{s}_j)$ and $\mathbf{C}_v(\boldsymbol{\theta}_v)$ is the corresponding

$n_s \times n_s$ spatial covariance matrix. Also, we assume linear fixed effects $\mu_z(\ell_i; \boldsymbol{\beta}_z) = \mathbf{q}_z(\ell_i)^\top \boldsymbol{\beta}_z$ and $\mu_y(\mathbf{s}_j; \boldsymbol{\beta}_y) = \mathbf{q}_y(\mathbf{s}_j)^\top \boldsymbol{\beta}_y$, where $\mathbf{q}_z(\ell_i)$ and $\mathbf{q}_y(\mathbf{s}_j)$ are $p_z \times 1$ and $p_y \times 1$ vectors of predictors or explanatory variables for $z(\ell_i)$ and $y(\mathbf{s}_j)$, respectively.

A joint Bayesian hierarchical model for $y(\mathbf{s}_j)$'s and $z(\ell_i)$'s, given measurements over \mathcal{S} and $\mathcal{S} \times \mathcal{X}$, respectively, is given by

$$\begin{aligned} p(\boldsymbol{\Theta}) &\times N(\boldsymbol{\beta}_y | \boldsymbol{\mu}_{\beta_y}, \mathbf{V}_{\beta_y}) \times N(\boldsymbol{\beta}_z | \boldsymbol{\mu}_{\beta_z}, \mathbf{V}_{\beta_z}) \times N(\boldsymbol{\alpha} | \boldsymbol{\mu}_{\alpha}, \mathbf{V}_{\alpha}) \times N(\mathbf{v} | \mathbf{0}, \mathbf{C}_v(\boldsymbol{\theta}_v)) \\ &\times N(\mathbf{u} | \mathbf{0}, \mathbf{C}_u(\boldsymbol{\theta}_u)) \times \prod_{j=1}^{n_s} N(y(\mathbf{s}_j) | \mathbf{q}_y^\top(\mathbf{s}_j) \boldsymbol{\beta}_y + \boldsymbol{\alpha}^\top \mathbf{u}(\mathbf{s}_j) + v(\mathbf{s}_j), \tau_y^2) \\ &\times \prod_{i=1}^n N(z(\ell_i) | \mathbf{q}_z^\top(\ell_i) \boldsymbol{\beta}_z + u(\ell_i), \tau_z^2(x_k)) , \end{aligned} \quad (5)$$

where $\boldsymbol{\Theta} = \{\boldsymbol{\theta}_u, \boldsymbol{\theta}_v, \tau_y^2, \tau_z^2\}$ with $\boldsymbol{\tau}_z^2 = (\tau_z^2(x_k))_{k=1}^{n_x}$, $\boldsymbol{\beta}_z$ and $\boldsymbol{\beta}_y$ are regression slopes for each $\mathbf{q}_z(\ell_i)$ and $\mathbf{q}_y(\mathbf{s}_i)$, respectively, $\mathbf{u}(\mathbf{s}_j)$ is the vector with elements $u(\mathbf{s}_j, x_k)$ for x_k 's in \mathcal{X} yielding LiDAR signals corresponding to \mathbf{s}_j , $\boldsymbol{\alpha}$ is an $n_x \times 1$ vector of unknown coefficients, viz. the $\alpha(x_j)$'s, for the elements in $\mathbf{u}(\mathbf{s}_i)$, and $p(\boldsymbol{\theta}_u)$ and $p(\boldsymbol{\theta}_v)$ are prior distributions on the process parameters for $u(\mathbf{s}, x)$ and $v(\mathbf{s})$, respectively. Further specifications customarily assume that

$$p(\boldsymbol{\Theta}) \propto p(\boldsymbol{\theta}_u) \times p(\boldsymbol{\theta}_v) \times IG(\tau_y^2 | a_{\tau_y}, b_{\tau_y}) \times \prod_{k=1}^{n_x} IG(\tau_z^2(x_k) | a_{\tau_z}, b_{\tau_z}) , \quad (6)$$

where $p(\boldsymbol{\theta}_u) = p(a, \gamma, c) \times IG(\sigma_u^2 | a_u, b_u)$ and $p(\boldsymbol{\theta}_v) = p(\phi_v) \times IG(\sigma_v^2 | a_v, b_v)$. When the number of space-height coordinates n is big, estimating (5) is computationally expensive and, depending upon the available computational resources, possibly unfeasible.

3.3 Predictive process counterparts for dimension reduction

To effectuate the computations necessary for estimating (5) when n is large, we will exploit reduced rank processes to achieve dimension reduction. Such processes usually arise as basis expansions of the original process with fewer number of basis functions than the number

of data points. This yields “low-rank” processes. Every choice of basis functions yields a process and there are far too many choices to enumerate here; see, e.g., Wikle (2010) for an excellent overview of these methods. Here, we opt for a particularly convenient choice, the predictive process (Banerjee et al. 2008), which derives the basis functions from taking the conditional expectation of the original process, often called the “parent” process, given its realizations over a fixed set of points, often referred to as “knots”. These knots are much smaller in number than the original number of points.

Let $\mathcal{S}_u^* = \{\mathbf{s}_{u,1}^*, \mathbf{s}_{u,2}^*, \dots, \mathbf{s}_{u,n_u^*}^*\}$ and $\mathcal{S}_v^* = \{\mathbf{s}_{v,1}^*, \mathbf{s}_{v,2}^*, \dots, \mathbf{s}_{v,n_v^*}^*\}$ be two sets of spatial knots to be used for constructing the predictive process counterparts of $u(\ell)$ and $v(\mathbf{s})$, respectively. Let $\mathcal{X}^* = \{x_1^*, x_2^*, \dots, x_{n_x^*}^*\}$ be a set of knots for heights in the LiDAR signal. We let $\mathcal{L}^* = \{\ell_1^*, \ell_2^*, \dots, \ell_{n_x^*}^*\}$ be an enumeration of the space-height knots, where each $\ell_i^* = (\mathbf{s}_{u,j}^*, x_k^*)$ for some $\mathbf{s}_{u,j}^* \in \mathcal{S}_u^*$ and $x_k^* \in \mathcal{X}^*$, and define

$$\begin{aligned}\tilde{u}(\ell) &= \mathbb{E}[u(\ell) | \{u(\ell_i^*)\}] = \sum_{i=1}^{n_u^*} b_{u,i}(\ell) u(\ell_i^*) \quad \text{and} \\ \tilde{v}(\mathbf{s}) &= \mathbb{E}[v(\mathbf{s}) | \{v(\mathbf{s}_{v,i}^*)\}] = \sum_{i=1}^{n_v^*} b_{v,i}(\mathbf{s}) v(\mathbf{s}_{v,i}^*).\end{aligned}\tag{7}$$

The $b_{u,i}(\ell)$ ’s and $b_{v,i}(\mathbf{s})$ ’s are basis functions derived from the respective conditional expectations in (7). Dimension reduction is achieved by choosing n^* and n_v^* to be much smaller than n and n_s , respectively. Even with data over n_s spatial locations and n_x heights so that $n = n_s n_x$, we need to work only with the $u(\ell_i^*)$ and $v(\mathbf{s}_i^*)$. Thus, we work with random vectors of dimensions n^* and n_v^* instead of n and n_s . If we choose $n^* = n$, $n_v^* = n_v$ and choose their respective knots to coincide with the original points, i.e., $\mathcal{S}_v^* = \mathcal{S}$ and $\mathcal{L}^* = \mathcal{L}$, then $\tilde{u}(\ell)$ and $\tilde{v}(\mathbf{s})$ coincide with $u(\ell)$ and $v(\mathbf{s})$, respectively.

For Gaussian processes, for any $\mathbf{s} \in \mathcal{D}$, the $b_{v,i}(\mathbf{s})$ ’s are the solution of $\mathbf{C}_v^*(\boldsymbol{\theta}_v) \mathbf{b}_v(\mathbf{s}) = \mathbf{c}_v^*(\mathbf{s})$, where $\mathbf{b}_v(\mathbf{s})$ is $n_v^* \times 1$ with i -th element $b_{v,i}(\mathbf{s})$, $\mathbf{C}_v^*(\boldsymbol{\theta}_v)$ is $n_v^* \times n_v^*$ with (i, j) -th element $C_v(\mathbf{s}_{v,i}^*, \mathbf{s}_{v,j}^*; \boldsymbol{\theta})$ and $\mathbf{c}_v^*(\mathbf{s})$ is $n_v^* \times 1$ with i -th entry $C_v(\mathbf{s}, \mathbf{s}_{v,i}^*; \boldsymbol{\theta}_v)$. Similarly, for any $\ell \in \mathcal{D} \times \mathcal{H}$, we solve the $n^* \times n^*$ system $\mathbf{C}_u^*(\ell) \mathbf{b}_u(\ell) = \mathbf{c}_u^*(\ell)$, where $\mathbf{b}_u(\ell)$ is $n^* \times 1$ with elements $b_{u,i}(\ell)$, $\mathbf{C}_u^*(\ell)$ is $n^* \times n^*$ with entries $C_u(\ell_i^*, \ell_j^*; \boldsymbol{\theta}_u)$, and $\mathbf{c}_u^*(\ell)$ is $n^* \times 1$ with entries $C_u(\ell, \ell_i^*)$.

The predictive process yields the variances of the residual processes $u(\ell) - \tilde{u}(\ell)$ and $v(\mathbf{s}) - \tilde{v}(\mathbf{s})$ as $\delta_u^2(\ell) = C_u[\ell, \ell] - \mathbf{c}_u^{*\top}(\ell) \mathbf{C}_u^{*-1}(\boldsymbol{\theta}_u) \mathbf{c}_u^*(\ell)$ and $\delta_v^2(\mathbf{s}) = C_v(\mathbf{s}, \mathbf{s}) - \mathbf{c}_v^{*\top}(\mathbf{s}) \mathbf{C}_v^{*-1}(\boldsymbol{\theta}_v) \mathbf{c}_v^*(\mathbf{s})$, respectively. To compensate for the smoothing caused by the reduced-rank models, we further construct independent processes $\tilde{\epsilon}_u(\ell) \stackrel{ind}{\sim} N(0, \delta_u^2(\ell))$ and $\tilde{\epsilon}_v(\mathbf{s}) \stackrel{ind}{\sim} N(0, \delta_v^2(\mathbf{s}))$ and employ $\tilde{u}(\ell) + \tilde{\epsilon}_u(\ell)$ and $\tilde{v}(\mathbf{s}) + \tilde{\epsilon}_v(\mathbf{s})$ for dimension reduction. This adjustment is called a “bias-adjustment” as it fixes an over-estimation of the variability at the origin by the reduced-rank processes and provides a better approximation to the parent process.

Replacing the processes in (5) with their predictive process counterparts and introducing the residual adjustments discussed above, produces the following reduced-rank Bayesian hierarchical model

$$\begin{aligned}
p(\boldsymbol{\Theta}) &\times N(\boldsymbol{\beta}_y \mid \boldsymbol{\mu}_{\beta_y}, \mathbf{V}_{\beta_y}) \times N(\boldsymbol{\beta}_z \mid \boldsymbol{\mu}_{\beta_z}, \mathbf{V}_{\beta_z}) \times N(\boldsymbol{\alpha} \mid \boldsymbol{\mu}_\alpha, \mathbf{V}_\alpha) \times N(\mathbf{v}^* \mid \mathbf{0}, \mathbf{C}_v^*(\boldsymbol{\theta}_v)) \\
&\times N(\mathbf{u}^* \mid \mathbf{0}, \mathbf{C}_u^*(\boldsymbol{\theta}_u)) \times \prod_{j=1}^{n_s} N(y(\mathbf{s}_j) \mid \mathbf{q}_y^\top(\mathbf{s}_j) \boldsymbol{\beta}_y + \boldsymbol{\alpha}^\top \mathbf{B}(\mathbf{s}_j) \mathbf{u}^* + \mathbf{b}_v^\top(\mathbf{s}_j) \mathbf{v}^*, d_y^2(\mathbf{s}_j)) \\
&\times \prod_{i=1}^n N\left(z(\ell_i) \mid \mathbf{q}_z(\ell_i)^\top \boldsymbol{\beta}_z + \sum_{j=1}^{n^*} b_{u,j}(\ell_i) u(\ell_j^*), d_z^2(\ell_i)\right), \tag{8}
\end{aligned}$$

where $p(\boldsymbol{\Theta})$ is as in (6), $d_z^2(\ell_i) = \tau_z^2(x_k) + \delta_u^2(\ell_i)$, $d_y^2(\mathbf{s}_j) = \tau_y^2 + \sum_{k=1}^{n_x} \alpha_k^2 \delta_u^2(\mathbf{s}_j, x_k) + \delta_v^2(\mathbf{s}_j)$, $\boldsymbol{\alpha}$ is as in (5), each $\mathbf{B}(\mathbf{s}_j)$ is $n_x \times n^*$ with (k, i) -th element $b_{u,i}(\mathbf{s}_j, x_k)$, \mathbf{u}^* is $n^* \times 1$ obtained by stacking the $u(\ell_j^*)$'s conformably with $\mathbf{B}(\mathbf{s}_j)$, \mathbf{v}^* is $n_v^* \times 1$ with elements $v(\mathbf{s}_{v,i}^*)$, and $\mathbf{C}_u^*(\boldsymbol{\theta}_u)$ and $\mathbf{C}_v^*(\boldsymbol{\theta}_v)$ are the covariance matrices for \mathbf{u}^* and \mathbf{v}^* , respectively. Further savings accrue if we let $\boldsymbol{\alpha}$ in (8) be $n_x^* \times 1$ with entries $\alpha(x_k^*)$, whence $\mathbf{B}(\mathbf{s}_j)$ is $n_x^* \times n^*$ with (k, i) -th element $b_{u,i}(\mathbf{s}_j, x_k^*)$. Letting $\mathcal{S}_v^* = \mathcal{S}$ and $\mathcal{L}^* = \mathcal{L}$ makes (8) equal to the full model (5).

We point out that further enhancements to the predictive process have been investigated by Sang and Huang (2012), who suggested improving the approximation by tapering the residual processes, and Katzfuss (2016), who proposed a multi-resolution predictive process by hierarchically partitioning the domain and nesting the residual process adjustments within these hierarchical structures. The latter considerably enhances the scalability of predictive

process models and can be used in our setting for even larger datasets. However, for the scale of our current application, the model in (8) is adequate.

4 Bayesian estimation and prediction

To estimate the model in (8), we resort to a Markov chain Monte Carlo (MCMC) algorithm for generating exact inference from the posterior distribution of all unknown parameters in (8). In order to expedite convergence, we use a “collapsed” model by integrating out \mathbf{u}^* and \mathbf{v}^* from (8). Let $\mathbf{B}_u(\boldsymbol{\theta}_u)$ be the $n \times n^*$ matrix with (i, j) -th element $b_{u,j}(\ell_i)$, $\mathbf{G}(\boldsymbol{\theta}_u, \boldsymbol{\alpha})$ be $n_s \times n^*$ with rows $\boldsymbol{\alpha}^\top \mathbf{B}(\mathbf{s}_i)$, $\mathbf{B}_v(\boldsymbol{\theta}_v)$ be $n_s \times n_v^*$ with (i, j) -th element $b_{v,j}(\mathbf{s}_{v,i}^*)$, $\mathbf{D}_y(\boldsymbol{\theta}_v, \boldsymbol{\theta}_u, \boldsymbol{\alpha}, \tau_y^2)$ be the diagonal matrix with elements $\tau_y^2 + \sum_{k=1}^{n_x} \alpha_k^2 \delta_u^2(\mathbf{s}_i, x_k) + \delta_v^2(\mathbf{s}_i)$ arranged conformably with $y(\mathbf{s}_i)$ ’s in \mathbf{y} and $\mathbf{D}_z(\boldsymbol{\theta}_u, \tau_z^2)$ be diagonal with $\tau_z^2(x_k) + \delta_u^2(\ell_i)$ arranged along the diagonal conformably with $z(\ell_i)$ ’s in \mathbf{z} . Then, $\mathbf{V}_z = \mathbf{B}_u(\boldsymbol{\theta}_u) \mathbf{C}_u^*(\boldsymbol{\theta}_u) \mathbf{B}_u(\boldsymbol{\theta}_u)^\top + \mathbf{D}_z(\boldsymbol{\theta}_u, \tau_z^2)$ is the $n \times n$ variance-covariance matrix for \mathbf{z} , $\mathbf{V}_y = \mathbf{G}(\boldsymbol{\theta}_u, \boldsymbol{\alpha}) \mathbf{C}_u^*(\boldsymbol{\theta}_u) \mathbf{G}(\boldsymbol{\theta}_u, \boldsymbol{\alpha})^\top + \mathbf{B}_v(\boldsymbol{\theta}_v) \mathbf{C}_v^*(\boldsymbol{\theta}_v) \mathbf{B}_v(\boldsymbol{\theta}_v)^\top + \mathbf{D}_y(\boldsymbol{\theta}_v, \boldsymbol{\theta}_u, \boldsymbol{\alpha}, \tau_y^2)$ is the $n_s \times n_s$ variance-covariance matrix for \mathbf{y} , and $\mathbf{V}_{zy} = \mathbf{B}_u(\boldsymbol{\theta}_u) \mathbf{C}_u^*(\boldsymbol{\theta}_u) \mathbf{G}^\top(\boldsymbol{\theta}_u, \boldsymbol{\alpha})$ is the $n \times n_s$ cross-covariance matrix between \mathbf{z} and \mathbf{y} , where \mathbf{z} is $n \times 1$ with elements $z(\ell_i)$, \mathbf{y} is $n_s \times 1$ with elements $y(\mathbf{s}_i)$. We write the model in terms of the above matrices as

$$\begin{aligned} p(\boldsymbol{\theta}_v) \times p(\boldsymbol{\theta}_u) \times N(\boldsymbol{\beta}_y | \boldsymbol{\mu}_{\beta_y}, \mathbf{V}_{\beta_y}) \times N(\boldsymbol{\beta}_z | \boldsymbol{\mu}_{\beta_z}, \mathbf{V}_{\beta_z}) \times N(\boldsymbol{\alpha} | \boldsymbol{\mu}_{\alpha}, \mathbf{V}_{\alpha}) \\ \times N(\mathbf{y} | \mathbf{Q}_y \boldsymbol{\beta}_y, \mathbf{V}_y) \times N(\mathbf{z} | \mathbf{Q}_z \boldsymbol{\beta}_z + \mathbf{V}_{zy} \mathbf{V}_y^{-1}(\mathbf{y} - \mathbf{Q}_y \boldsymbol{\beta}_y), \mathbf{V}_z - \mathbf{V}_{zy} \mathbf{V}_y^{-1} \mathbf{V}_{zy}^\top) , \end{aligned} \quad (9)$$

where \mathbf{Q}_z is $n \times p_z$ with rows $\mathbf{q}_z^\top(\ell_i)$ stacked conformably with \mathbf{z} and \mathbf{Q}_y is $n_s \times p_y$ with rows $\mathbf{q}_y^\top(\mathbf{s}_i)$ stacked conformably with \mathbf{y} .

We use random-walk Metropolis steps to update the parameters $\{\boldsymbol{\theta}_u, \boldsymbol{\theta}_v, \boldsymbol{\alpha}, \tau_y^2, \tau_z^2\}$ as one block which requires evaluating the multivariate Gaussian likelihoods in (9) and will benefit from efficient numerical linear algebra for the inverse and determinant of the variance covariance matrices. We can accomplish this effectively using two functions: $\mathbf{L} = \text{chol}(\mathbf{M})$ which computes the Cholesky factorization for a positive definite matrix $\mathbf{M} = \mathbf{L} \mathbf{L}^\top$, where

\mathbf{L} is lower-triangular, and $\mathbf{X} = \text{trsolve}(\mathbf{T}, \mathbf{B})$ which solves the triangular system $\mathbf{TX} = \mathbf{B}$ for a triangular (lower or upper) matrix \mathbf{T} . Further details follow.

The joint density for \mathbf{y} and \mathbf{z} in (9) is, in fact, $N(\mathbf{w} | \mathbf{Q}\boldsymbol{\beta}, \mathbf{AJA}^\top + \mathbf{D})$, where \mathbf{w} is the $(n + n_s) \times 1$ vector obtained by stacking \mathbf{z} over \mathbf{y} , \mathbf{Q} is block diagonal with blocks \mathbf{Q}_z and \mathbf{Q}_y , $\boldsymbol{\beta}$ is $(p_z + p_y) \times 1$ obtained by stacking $\boldsymbol{\beta}_z$ over $\boldsymbol{\beta}_y$, \mathbf{A} is $(n + n_s) \times (n^* + n_v^*)$ partitioned into a 2×2 block matrix with first row $\begin{bmatrix} \mathbf{B}_u(\boldsymbol{\theta}_u) : \mathbf{O} \end{bmatrix}$ and second row $\begin{bmatrix} \mathbf{G}(\boldsymbol{\theta}_u, \boldsymbol{\alpha}) : \mathbf{B}_v(\boldsymbol{\theta}_v) \end{bmatrix}$, \mathbf{J} is block diagonal with blocks $\mathbf{C}_u^*(\boldsymbol{\theta}_u)$ and $\mathbf{C}_v^*(\boldsymbol{\theta}_v)$, and \mathbf{D} is block diagonal with blocks $\mathbf{D}_z(\boldsymbol{\theta}_u, \tau_z^2)$ and $\mathbf{D}_y(\boldsymbol{\theta}_v, \boldsymbol{\theta}_u, \boldsymbol{\alpha}, \tau_y^2)$. We now compute

$$(\mathbf{AJA}^\top + \mathbf{D})^{-1} = \mathbf{D}^{-1/2}(\mathbf{I} - \mathbf{H}^\top \mathbf{H})\mathbf{D}^{-1/2}, \quad (10)$$

where \mathbf{H} is obtained by first computing $\mathbf{W} = \mathbf{D}^{-1/2}\mathbf{A}$, then the Cholesky factorization $\mathbf{L} = \text{chol}(\mathbf{J}^{-1} + \mathbf{W}^\top \mathbf{W})$, and finally solving the triangular system $\mathbf{H} = \text{trsolve}(\mathbf{L}, \mathbf{W}^\top)$. Having obtained \mathbf{H} , we compute $\mathbf{e} = \mathbf{w} - \mathbf{Q}\boldsymbol{\beta}$, $\mathbf{m} = \mathbf{D}^{-1/2}\mathbf{e}$, $\mathbf{N} = \mathbf{H}\mathbf{m}$, and obtain $\mathbf{T} = \text{chol}(\mathbf{I}_{n^*} - \mathbf{H}\mathbf{H}^\top)$. The log-target density for $\{\boldsymbol{\theta}_u, \boldsymbol{\theta}_v, \boldsymbol{\alpha}, \tau_y^2, \tau_z^2\}$ is then computed as

$$\begin{aligned} \log p(\boldsymbol{\theta}_u) + \log p(\boldsymbol{\theta}_v) + \log p(\tau_y^2) + \sum_{k=1}^{n_x} \log p(\tau_z^2(x_k)) - \frac{1}{2}(\boldsymbol{\alpha} - \boldsymbol{\mu}_\alpha)^\top \mathbf{V}_\alpha^{-1}(\boldsymbol{\alpha} - \boldsymbol{\mu}_\alpha) \\ - \frac{1}{2} \sum_{i=1}^{n+n_s} d_{ii} + \sum_{i=1}^{n^*+n_v^*} \log t_{ii} - \frac{1}{2}(\mathbf{m}^\top \mathbf{m} - \mathbf{N}^\top \mathbf{N}), \end{aligned} \quad (11)$$

where d_{ii} 's and t_{ii} 's are the diagonal elements of \mathbf{D} and \mathbf{T} , respectively. The total number of flops required for evaluating the target is $O((n + n_s)(n^* + n_v^*)^3) \approx O(nn^*3)$ (since $n \gg n_s$ and typically we choose $n^* \gg n_v^*$) which is considerably cheaper than the $O(n^3)$ flops that would have been required for the analogous computations in (5). In practice, Gaussian proposal distributions are employed for the Metropolis algorithm and all parameters with positive support are transformed to their logarithmic scale. Therefore, the necessary jacobian adjustments are made to (11) by adding some scalar quantities which is negligible in terms of computational costs.

Starting with initial values for all parameters, each iteration of the MCMC executes the above calculations to provide a sample for $\{\boldsymbol{\theta}_u, \boldsymbol{\theta}_v, \boldsymbol{\alpha}, \tau_y^2, \tau_z^2\}$. The regression parameter $\boldsymbol{\beta}$ is then sampled from its full conditional distribution. If $\mathbf{V}_w = \mathbf{AJA}^T + \mathbf{D}$ as in (10), $\boldsymbol{\mu}_\beta$ is $(p_z + p_y) \times 1$ with $\boldsymbol{\mu}_{\beta_z}$ stacked over $\boldsymbol{\mu}_{\beta_y}$ and \mathbf{V}_β is block diagonal with blocks \mathbf{V}_{β_z} and \mathbf{V}_{β_y} , then the full conditional distribution for $\boldsymbol{\beta}$ is $N(\mathbf{B}\mathbf{b}, \mathbf{B})$, where $\mathbf{B}^{-1} = \mathbf{V}_\beta^{-1} + \mathbf{Q}^\top \mathbf{V}_w^{-1} \mathbf{Q}$ and $\mathbf{b} = \mathbf{V}_\beta^{-1} \boldsymbol{\mu}_\beta + \mathbf{Q}^\top \mathbf{V}_w^{-1} \mathbf{w}$. These are efficiently computed as $[\mathbf{x} : \mathbf{X}] = \mathbf{D}^{-1/2} [\mathbf{y} : \mathbf{Q}]$, $\tilde{\mathbf{X}} = \mathbf{H}\mathbf{X}$ and setting $\mathbf{b} = \mathbf{V}_\beta^{-1} \boldsymbol{\mu}_\beta + \mathbf{X}^T \mathbf{x} - \tilde{\mathbf{X}}^T \mathbf{H}\mathbf{x}$ and $\mathbf{L}_B = \text{chol}(\mathbf{V}_\beta^{-1} + \mathbf{X}^T \mathbf{X} - \tilde{\mathbf{X}}^T \tilde{\mathbf{X}})$. We then set $\boldsymbol{\beta} = \text{trsolve}(\mathbf{L}_B^T, \text{trsolve}(\mathbf{L}_B, \mathbf{b})) + \text{trsolve}(\mathbf{L}_B, \tilde{\mathbf{z}})$, where $\tilde{\mathbf{z}}$ is a conformable vector of independent $N(0, 1)$ variables.

We repeat the above computations for each iteration of the MCMC algorithm using the current values of the process parameters in \mathbf{V}_w . The algorithm described above will produce, after convergence, posterior samples for $\boldsymbol{\Omega} = \{\boldsymbol{\theta}_u, \boldsymbol{\alpha}, \boldsymbol{\theta}_v, \tau_y^2, \tau_z^2, \boldsymbol{\beta}_y, \boldsymbol{\beta}_z\}$. We can subsequently obtain the posterior samples for \mathbf{u}^* and \mathbf{v}^* using exact sampling. To be precise, if \mathbf{g} is the $(n^* + n_v^*) \times 1$ vector with \mathbf{u}^* stacked over \mathbf{v}^* , then we seek samples from its posterior predictive distribution

$$p(\mathbf{g} | \mathbf{y}, \mathbf{z}) = \int p(\mathbf{g} | \boldsymbol{\Omega}, \mathbf{y}, \mathbf{z}) p(\boldsymbol{\Omega} | \mathbf{y}, \mathbf{z}) d\boldsymbol{\Omega}, \quad (12)$$

where $p(\mathbf{g} | \boldsymbol{\Omega}, \mathbf{y}, \mathbf{z})$ is $N(\mathbf{B}\mathbf{b}, \mathbf{B})$, where $\mathbf{B} = (\mathbf{J}^{-1} + \mathbf{A}^\top \mathbf{D}^{-1} \mathbf{A})^{-1}$ and $\mathbf{b} = \mathbf{A}^\top \mathbf{D}^{-1} (\mathbf{w} - \mathbf{Q}\boldsymbol{\beta})$. Since $n^* + n_v^*$ is chosen to be much smaller than $n + n_s$, obtaining $\text{chol}(\mathbf{B})$ is not as expensive, but can produce numerical instabilities due to the inverses of $\mathbf{C}_u^*(\boldsymbol{\theta}_u)$ and $\mathbf{C}_v^*(\boldsymbol{\theta}_v)$ appearing in \mathbf{J}^{-1} which we seek to avoid. We execute a numerically stable algorithm exploiting the fact that $\mathbf{B} = \mathbf{K} - \mathbf{K}(\mathbf{J} + \mathbf{K})^{-1}\mathbf{K}$, where $\mathbf{K}^{-1} = \mathbf{A}^\top \mathbf{D}^{-1} \mathbf{A}$. For each posterior sample of $\boldsymbol{\Omega}$, we compute $\mathbf{L} = \text{chol}(\mathbf{J} + \mathbf{K})$, $\mathbf{W} = \text{trsolve}(\mathbf{L}, \mathbf{K})$ and $\mathbf{L}_B = \mathbf{K} - \mathbf{W}^\top \mathbf{W}$. We generate an $(n^* + n_v^*) \times 1$ vector $\mathbf{z}^* \sim N(\mathbf{0}, \mathbf{I}_{n^* + n_v^*})$ and set $\mathbf{g} = \mathbf{L}_B(\mathbf{z}^* + \mathbf{L}_B^\top \mathbf{b})$. Repeating this for every posterior sample of $\boldsymbol{\Omega}$, produces the posterior predictive samples for \mathbf{g} from (12) and, hence, those for \mathbf{u}^* and \mathbf{v}^* .

Finally, we seek predictive inference for $z(\ell_0)$ at any arbitrary space-height coordinate ℓ_0 and for $y(\mathbf{s}_0)$ at any arbitrary spatial location \mathbf{s}_0 . Given $\mathbf{q}_z^\top(\ell_0)$ and $\mathbf{q}_y^\top(\mathbf{s}_0)$, we draw

$$z(\ell_0) \sim N \left(\mathbf{q}_z^\top(\ell_0) \boldsymbol{\beta}_z + \sum_{j=1}^{n^*} b_{u,j}(\ell_0) u(\ell_j^*), d_z^2(\ell_0) \right) \text{ and} \quad (13)$$

$$y(\mathbf{s}_0) \sim N \left(\mathbf{q}_y^\top(\mathbf{s}_0) \boldsymbol{\beta}_y + \boldsymbol{\alpha}^\top \mathbf{B}(\mathbf{s}_0) \mathbf{u}^* + \mathbf{b}_v^\top(\mathbf{s}_0) \mathbf{v}^*, d_y^2(\mathbf{s}_0) \right) . \quad (14)$$

Repeating for every posterior sample of $\boldsymbol{\Omega}$, \mathbf{v}^* and \mathbf{u}^* yields the corresponding posterior predictive samples for $z(\ell_0)$ and $y(\mathbf{s}_0)$. Posterior predictive samples of the latent processes can also be easily computed as $u(\ell_0) = \sum_{j=1}^{n^*} b_{u,j}(\ell_0) u(\ell_j^*)$ and $v(\mathbf{s}_0) = \mathbf{b}_v^\top(\mathbf{s}_0) \mathbf{v}^*$ for each posterior sample of the $u(\ell_j^*)$'s, \mathbf{v}^* and the process parameters present in the basis functions $b_{u,j}(\ell_0)$ and $\mathbf{b}_v^\top(\mathbf{s}_0)$. Posterior predictive distributions at observed locations and space-height coordinates yield *replicated* data (see, e.g., Gelman et al. 2013) that we use for model assessment and comparisons in Section 5.

5 Data analysis

The proposed MCMC sampler and prediction algorithms were implemented in C++ (all code provided in the supplemental web material). The matrix computations described in Section 4 were efficiently implemented with threaded BLAS and LAPACK libraries in Intel's Math Kernel Library. Posterior inference for subsequent analysis were based upon three chains of 50000 iterations (with a burn-in of 10000 iterations). The computations were conducted on a Linux workstation using two Intel Nehalem quad-Xeon processors.

In the subsequent simulation experiment Section 5.1 and PEF data analysis Section 5.2 candidate models were compared based on parameter estimates, fit to the observed data, out-of-sample prediction, and posterior predictive distribution coverage. Model choice was assessed using the deviance information criterion or DIC and model complexity p_D (Spiegelhalter et al. 2002) and a posterior predictive loss criterion D=G+P (Gelfand and Ghosh 1998), where smaller values of DIC and D indicate preferred models. For both analyses, a

25% holdout set, comprising locations selected at random, served to assess out-of-sample prediction. Prediction accuracy for the holdout locations was measured using root mean squared prediction error (RMSPE) (Yeniyay and Goktas 2002) as well as CRPS and GRS given in Equation 21 and 27, respectively, in Gneiting and Raftery (2007). Smaller values RMSPE and CRPS, and larger values of GRS, indicate improved predictive ability. The percent of holdout locations that fell within their respective posterior predictive distribution 95% CI was also computed along with the average interval width.

5.1 Simulation experiment

Using the *true* parameter values given in the first column of Table 1 and Figure 2, we simulated AGB and LiDAR signals from the full GP joint likelihood for AGB and LiDAR in (5) for $n_s = 400$ coinciding locations in \mathcal{S} on a regular grid within a $[0, 4] \times [0, 4]$ domain and $n_x = 50$ heights within $[0, 5]$. The AGB signal was regressed on a global intercept (β_y) while the LiDAR signals were regressed on the 50 height-specific intercepts and non-spatial variances; thus $\boldsymbol{\beta}_z$ and $\boldsymbol{\tau}_z^2$ are both 50×1 . A subset of 100 locations from the 400 were withheld to assess out-of-sample predictions. Each of our candidate predictive process models used $n_x^* = 5$ equally spaced knots for height in the $[0, 5]$ interval and $n_v^* = n_s = 300$ with $\mathcal{S}_v^* = \mathcal{S}$. Candidate models differed on the number of knots n_u^* . We considered models with $n_u^* = 300$ and $\mathcal{S}_u^* = \mathcal{S}$ in (8) and with n_u^* equaling 200, 100, and 50 knots, respectively, selected on a regular grid within the domain.

Parameter estimates and performance metrics for all candidate models are given in Table 1. With the exception of α_3 for n_u^* equal to 200 and 100, and a few of the covariance parameters for n_u^* equal to 100 and 50, the 95% CIs for all parameters included the *true* values. Importantly, the α estimates—used to relate information between LiDAR signals and AGB—remain consistent in sign and magnitude as the spatial process associated with the signals is modeled over a reduced number of knots. Figure 2 provides the posterior summaries for the 50 height-specific intercepts and non-spatial variances associated with the LiDAR signals; results for only two candidate models are provided due to the large number

Table 1: Parameter credible intervals, 50% (2.5%, 97.5%), goodness-of-fit, and predictive validation. Bold entries indicate where the true value is missed, bold goodness-of-fit metrics indicate *best* fit, and bold prediction metrics indicate *best* predictive performance.

Parameter	True	Models		
		$n_u^* = 300$ and $\mathcal{S}_u^* = \mathcal{S}$	$n_u^* = 200$	$n_u^* = 100$
β_y	20	20.11(19.3,21.06)	20.21(19.48,21.05)	20.28(19.46,21.32)
α_1	-2	-1.92(-2.25,-1.61)	-2.09(-2.49,-1.73)	-2.03(-2.63,-1.45)
α_2	0	0.06(-0.3,0.46)	0.38(-0.13,0.83)	0.25(-0.62,1.03)
α_3	2	1.57(1.06,2.01)	1.21 0.71,1.77	1.12 0.26,1.99
α_4	1	0.91(0.54,1.29)	0.77(0.34,1.19)	0.93(0.26,1.6)
α_5	5	4.94(4.64,5.23)	4.9(4.52,5.27)	4.82(4.23,5.43)
σ_u^2	0.2	0.2(0.19,0.22)	0.21(0.2,0.22)	0.22 0.21,0.23
a	12	12.91(11.62,14.46)	11.53(10.1,13.36)	10.58(9.29,12.63)
γ	0.9	0.89(0.84,0.93)	0.94(0.85,0.97)	0.92(0.83,0.97)
c	5	5.17(4.62,5.93)	5.24(4.75,5.87)	3.82 3.35,4.29
σ_v^2	0.5	0.64(0.34,1.27)	0.68(0.37,1.24)	0.51(0.15,1.47)
ϕ_v	2	1.68(0.41,3.87)	1.7(0.49,3.8)	1.38(0.21,5.26)
p_D for AGB & LiDAR		95.01	95.94	96.14
DIC for AGB & LiDAR		28399.73	29238.34	30140.16
G for AGB & LiDAR		6883.54	7705.30	8566.07
P for AGB & LiDAR		7507.49	8215.54	9007.16
D=G+P for AGB & LiDAR		14391.03	15920.84	17573.23
RMSPE for AGB & LiDAR		0.80	0.80	0.81
CRPS for AGB & LiDAR		2054.52	2056.32	2076.22
GRS for AGB & LiDAR		-712.04	-743.83	-864.92
95% prediction interval coverage for AGB& LiDAR %	95.27	95.1	95.39	18165.43
RMSPE for AGB observed LiDAR		2.79	2.74	2.78
CRPS for AGB observed LiDAR		159.32	156.28	157.71
GRS for AGB observed LiDAR		-311.06	-305.18	-308.63
95% prediction interval coverage for AGB observed LiDAR %	89	91	93	93
95% prediction interval width for AGB observed LiDAR	9.30	9.70	9.74	9.96
CPU time	101.7 h	60.0 h	27.5 h	13.8 h

of parameters and minimal difference in estimates among the models. These estimates also seem robust to a coarser representation of the underlying process (Figure 2).

Not surprisingly, for the joint outcome vector, goodness-of-fit and out-of-sample prediction is best for the full model, i.e., $n_u^* = 300$ (rows labeled AGB & LiDAR in Table 1). Interestingly, in an interpolation setting when LiDAR is observed, AGB prediction improves slightly when moving from the full model to the $n_u^* = 200$ knot model (rows labeled AGB | observed LiDAR in Table 1). In general, goodness-of-fit and predictive performance is not substantially degraded for the predictive process models when compared to the full model. The last row in Table 1 gives the CPU time for the candidate models. A 6-fold decrease in knots between the full model and $n_u^* = 50$ knot model results in a 7-fold decrease in computing time.

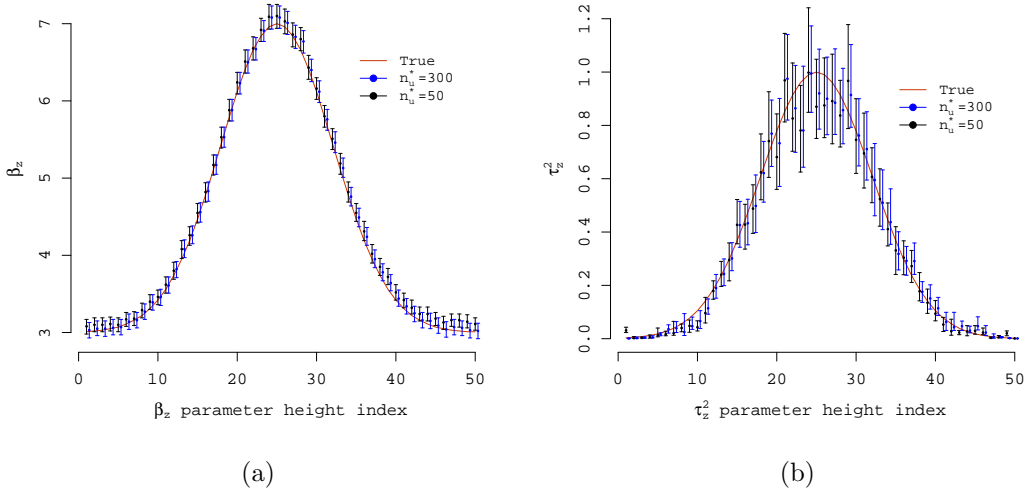


Figure 2: Parameter posterior summaries, 50% point symbol and 95% credible interval bars. Posterior summaries are jittered slightly along the x-axis to facilitate comparison.

5.2 Forest LiDAR and biomass data analysis

5.2.1 Data preparation

Pre-processing the raw G-LiHT LiDAR data followed methods detailed in Cook et al. (2013) and produced a complete 15×15 m grid across the PEF, where each pixel contained

a LiDAR signal. Prior to analysis, these LiDAR signals were further processed to remove excess zeros and coarsened to remove small-scale noise. Specifically, the maximum tree height across the PEF was approximately 22.8 m and hence LiDAR signal values beyond this height were zero and subsequently removed. Small-scale anomalies that occurred across each signal's 113 values were smoothed by averaging every two consecutive measurements. Truncation above forest canopy extent and smoothing resulted in signals of length $n_x = 39$ within the $[0, 22.8]$ m height interval. Figure 1(b) illustrates the processed signals over the PSPs within two MUs.

As described in Section 1, important current and future LiDAR acquisition missions sparsely sample the domain of interest. The sampling designs, e.g., transects or clusters, aim to collect LiDAR data across the domain and also at forest inventory plot locations. To mimic the sparseness of these anticipated datasets and associated inferential challenges, only LiDAR signals that spatially coincided with PSPs were used for candidate model parameter estimation. Also, to gain a better sense of shared information between LiDAR signals and AGB, and to further mimic anticipated worst-case settings, we do not include predictor variables in candidate model means.

5.2.2 Candidate models and results

Candidate models were formed by varying n_x^* , n_u^* , and n_v^* along with knot location following the approximately optimal knot design criteria described in the supplemental web material. We present results for n_x^* from 2 to 7, n_u^* equal 339 and 170, and $n_v^* = 339$. As in the simulated data analysis, AGB has a global intercept (β_y) and LiDAR has height-specific intercepts (so β_z is 39×1). To better assess the information contribution of latent LiDAR regressors for AGB prediction an additional set of models were fit with $v(\mathbf{s})$ set to zero (results presented in the supplemental web material). All candidate models were fit using a subset of $n_s = 339$ PSPs selected at random from the complete set of 451 PSPs. The remaining 202 PSP were used for out-of-sample prediction validation. Observed and holdout PSPs along with knot locations are illustrated in Figure 3. Here too, an example transect

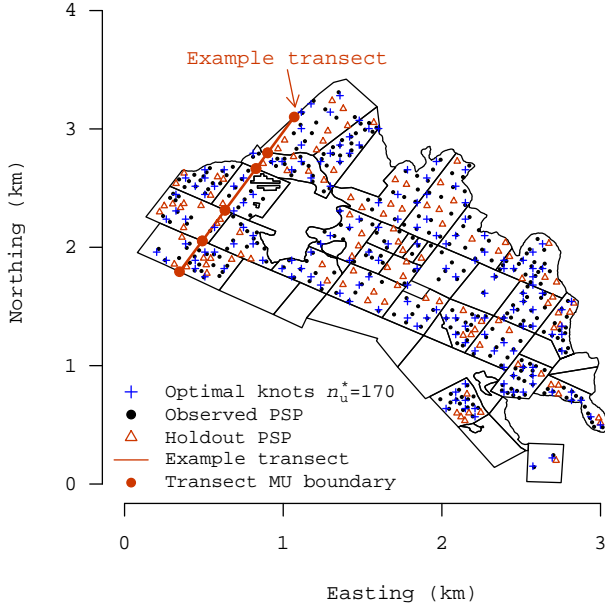


Figure 3: Locations of observed and holdout PSPs, predictive process knots, and illustrative transect on the PEF.

is identified along with locations where the transect crosses MU boundaries. This example transect is used to help visualize and assess results.

Parameter estimates and goodness-of-fit metrics for the afore mentioned choices of n_x^* are provided in Tables 2 and 3 for n_u^* equal 339 and 170, respectively. For both choices of n_u^* , increasing the number of height knots n_x^* resulted in improved fit (noted by lower values of DIC and D). This makes sense because a greater number of knots provides an improved representation of the LiDAR signal. This result also holds for candidate models that exclude the spatial process capturing features not shared between AGB and LiDAR, i.e., $v(\mathbf{s}) = 0$ (results in web material). Figure 4 provides posterior summaries for the LiDAR signal's height-specific intercept and non-spatial variance parameter estimates for two candidate models. Here, unlike the synthetic data analysis, there are some differences between parameter estimates at different levels of n_u^* . Specifically, we see more precises

estimates of the intercept parameters and lower residual variances for $n_u^* = 339$ across heights. This is not surprising, given the additional information about the signal supplied by the higher resolution spatial process representation.

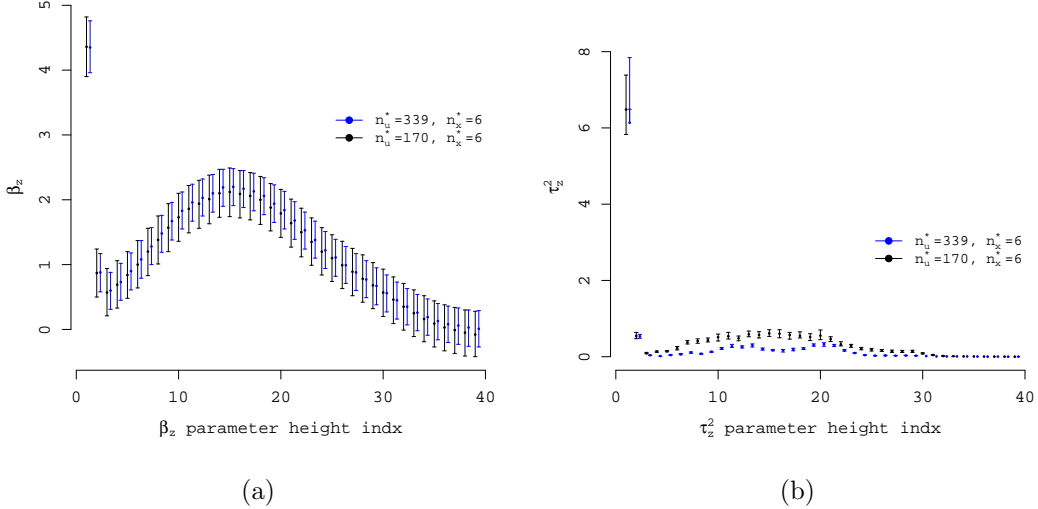


Figure 4: Parameter posterior summaries, 50% point symbol and 95% credible interval bars. Posterior summaries are jittered slightly along the x-axis to facilitate comparison.

Inference on α which acts as weights for the LiDAR process, help us gauge the impact of the latent LiDAR regressors. The increasing subscript value on α 's in Tables 2 and 3 correspond to increasing knot heights in \mathcal{X}^* . Regardless of the choice for n_u^* or n_v^* , estimates of α and knot height are positively associated. For example, estimates of α for the $n_x^* = 6$ model in Table 2 increase from α_1 (corresponding to knot x_1^* which is near the ground) to α_6 (corresponding to x_6^* which is near the maximum forest canopy height). The intuition here is that the latent LiDAR process $\tilde{u}(\ell)$ tend to have larger values at heights where energy return is large (i.e., where the signal encounters tree material such as leaves, branches, boles) and small where energy return is low (i.e., where there is mostly empty space in the vertical profile of the forest). Typically, more mature forests with large diameter and tall trees have higher AGB compared with younger lower canopy or sparsely populated forests. Therefore, we expect greater AGB in regions returning much of the LiDAR signal from greater heights

Table 2: Parameter credible intervals, 50% (2.5%, 97.5%), and goodness-of-fit for the $n_u^* = 339$ and $n_v^* = 339$ models. Bold parameter values indicated values that differ from zero where appropriate and bold goodness-of-fit metrics indicate *best* fit.

Parameter	Height knot models					
	$n_x^* = 2$	$n_x^* = 3$	$n_x^* = 4$	$n_x^* = 5$	$n_x^* = 6$	$n_x^* = 7$
β_y	1.04(0.87,1.23)	1.07(0.78,1.39)	1.04(0.9,1.2)	1.05(0.88,1.23)	1.05(0.86,1.24)	1.04(0.89,1.2)
α_1	-0.08(-0.14,0.01)	-0.09(-0.2,0.01)	-0.04(-0.09,0)	0.02(-0.04,0.07)	-0.05(-0.12,0.01)	-0.05(-0.11,0.01)
α_2	0.32(0.27,0.38)	0.01(-0.19,0.22)	-0.16(-0.23,0.1)	-0.05(-0.13,0.03)	-0.12(-0.19,-0.04)	-0.08(-0.17,-0.01)
α_3	-	0.42(0.31,0.53)	0.11(0.06,0.18)	0.06(-0.02,0.13)	-0.11(-0.18,-0.04)	-0.1(-0.18,-0.04)
α_4	-	-	0.26(0.14,0.36)	0.2(0.13,0.26)	0.03(-0.04,0.11)	-0.02(-0.1,0.05)
α_5	-	-	-	0.32(0.16,0.45)	0.11(0.03,0.19)	0.06(-0.02,0.14)
α_6	-	-	-	-	0.2(0.0,0.39)	0.16(0.04,0.27)
α_7	-	-	-	-	-	0.03(-0.19,0.21)
σ_u^2	0.11(0.1,0.11)	0.15(0.14,0.17)	0.48(0.45,0.52)	0.62(0.58,0.67)	0.99(0.9,1.1)	0.97(0.91,1.03)
a	1.23(1.09,1.36)	1.41(1.26,1.55)	0.78(0.73,0.83)	1.13(1.07,1.2)	1.18(1.09,1.29)	1.04(0.99,1.09)
γ	1(1,1)	0.99(0.98,1)	0.99(0.97,1)	0.99(0.98,0.99)	1(1,1)	0.99(0.99,1)
c	17.73(15.28,21.53)	11.61(10.46,12.88)	8.98(8.3,9.8)	8.93(8.36,9.54)	7.72(7.18,8.33)	8.31(7.78,8.88)
σ_v^2	0.1(0.07,0.15)	0.15(0.1,0.22)	0.07(0.05,0.1)	0.08(0.05,0.11)	0.09(0.06,0.12)	0.08(0.06,0.11)
ϕ_v	3.47(1.9,5.93)	2.01(1.4,4.75)	3.67(2.41,5.35)	4.24(2.63,5.57)	3.42(1.96,4.02)	5.02(2.36,7.99)
τ_y^2	0.03(0.02,0.04)	0.03(0.02,0.04)	0.03(0.02,0.04)	0.03(0.02,0.04)	0.03(0.02,0.04)	0.02(0.02,0.04)
p_D	72.83	75.77	66.55	64.72	66.36	62.87
DIC	25394.17	24108.86	19561.92	15282.15	12766.62	9669.22
G	10492.42	8488.55	7009.5	4549.5	3724.98	3251.79
P	10864.7	8967.3	7714.91	5122.17	4284.75	3623.49
D=G+P	21357.12	17455.86	14724.41	9671.68	8009.73	6875.27

Table 3: Parameter credible intervals, 50% (2.5%, 97.5%), and goodness-of-fit for the $n_u^* = 170$ and $n_v^* = 339$ models. Bold parameter values indicated values that differ from zero where appropriate and bold goodness-of-fit metrics indicate *best* fit.

Parameter	Height knot models					
	$n_x^* = 2$	$n_x^* = 3$	$n_x^* = 4$	$n_x^* = 5$	$n_x^* = 6$	$n_x^* = 7$
β_y	1.03(0.81,1.25)	1.04(0.71,1.39)	1.04(0.9,1.19)	1.05(0.85,1.25)	1.06(0.81,1.31)	1.05(0.78,1.34)
α_1	-0.22(-0.43,-0.02)	-0.46(-0.67,-0.19)	-0.03(-0.15,0.1)	-0.04(-0.17,0.12)	-0.13(-0.28,0.03)	-0.11(-0.28,0.08)
α_2	0.73(0.55,0.9)	-0.54(-0.85,-0.1)	-0.26(-0.46,-0.07)	-0.23(-0.4,-0.05)	-0.12(-0.29,0.03)	-0.1(-0.24,0.04)
α_3	-	0.59(0.38,0.83)	0.24(0.06,0.42)	-0.09(-0.26,0.09)	-0.26(-0.42,-0.12)	-0.21(-0.37,-0.02)
α_4	-	-	0.28(0.08,0.5)	0.26(0.12,0.44)	0.09(-0.09,0.28)	-0.08(-0.23,0.06)
α_5	-	-	-	0.12(-0.2,0.42)	0.12(-0.08,0.3)	0.16(-0.01,0.38)
α_6	-	-	-	-	0.13(-0.31,0.47)	0.06(-0.13,0.29)
α_7	-	-	-	-	-	0.13(-0.2,0.5)
σ_u^2	0.05(0.05,0.06)	0.08(0.07,0.09)	0.26(0.23,0.28)	0.37(0.33,0.41)	0.41(0.37,0.46)	0.44(0.4,0.5)
a	0.73(0.58,0.91)	1.08(0.92,1.32)	0.85(0.77,0.94)	1.21(1.11,1.34)	1.24(1.13,1.37)	1.51(1.37,1.66)
γ	0.99(0.98,1)	0.99(0.94,1)	1(0.99,1)	1(0.99,1)	0.99(0.98,0.99)	0.99(0.98,1)
c	6.75(6.06,7.49)	5.13(4.53,5.8)	3.36(3.03,3.73)	3.1(2.78,3.43)	2.82(2.54,3.14)	3(2.68,3.34)
σ_v^2	0.09(0.06,0.16)	0.11(0.05,0.22)	0.05(0.04,0.08)	0.06(0.04,0.1)	0.07(0.05,0.11)	0.07(0.05,0.16)
ϕ_v	2.42(1.43,4.99)	1.59(0.94,4.68)	4.65(3.03,7.33)	3.5(2.01,5.89)	2.95(1.46,6.01)	2.67(1.23,6.72)
τ_2	0.03(0.02,0.05)	0.03(0.01,0.04)	0.03(0.02,0.05)	0.03(0.02,0.04)	0.03(0.02,0.05)	0.03(0.02,0.05)
p_D	79.27	78.95	73.86	68.84	70.81	72.06
DIC	2728.67	26426.63	24557.72	22929.39	22393.55	21962.06
G	11022.24	9777.49	8133.86	6743.01	6476.55	6154.11
P	11298.15	10112.78	8516.51	7207.75	6908.56	6554.33
D=G+P	22320.39	19890.27	16650.37	13950.76	13385.11	12708.44

and, conversely, lower AGB in regions returning much of the signal at lower heights.

Tables 4 and 5 provide out-of-sample prediction validation results corresponding to the models presented in Tables 2 and 3, respectively. For each level of n_u^* , RMSPE favors $n_x^* = 7$ whereas selection results based on CRPS and CRS are mixed. Importantly, however, holdout validation results suggest there is very little difference in predictive ability among the range of height knots beyond $n_x^* = 2$ or 3. If interest is in predicting AGB alone without also observing the LiDAR, the majority of the prediction metrics favor n_x^* between 4 and 7 as indicated in the lower portion of Tables 4 and 5 (note, these metrics are not based on the conditional prediction of AGB given the LiDAR at a location, i.e., interpolation, but rather for AGB from the joint prediction with LiDAR).

Table 4: Prediction metrics for the $n_u^* = 339$ and $n_v^* = 339$ models. Bold values indicate *best* predictive performance.

Parameter	Height knot models					
	$n_x^* = 2$	$n_x^* = 3$	$n_x^* = 4$	$n_x^* = 5$	$n_x^* = 6$	$n_x^* = 7$
RMSPE for AGB & LiDAR	0.89	0.855	0.833	0.784	0.775	0.771
CRPS for AGB & LiDAR	1972.57	1908.42	1863.4	1772.23	1778.66	1789.73
GRS for AGB & LiDAR	-2129.19	-1589.73	-1500.15	-1168.25	-1261.61	-1432.38
95% prediction coverage for AGB & LiDAR	93	93.3	93.7	93.6	94.5	95.1
RMSPE for AGB	0.324	0.319	0.317	0.316	0.317	0.317
CRPS for AGB	20.57	20.05	19.96	19.87	19.9	19.9
GRS for AGB	129.64	142.56	145.1	146.74	146.85	146.57
95% prediction interval coverage for AGB	89.3	92.9	93.8	94.6	94.6	93.8
95% prediction interval width for AGB	1.01	1.09	1.14	1.27	1.23	1.21

Table 5: Prediction metrics for the $n_u^* = 170$ and $n_v^* = 339$ models. Bold values indicate *best* predictive performance.

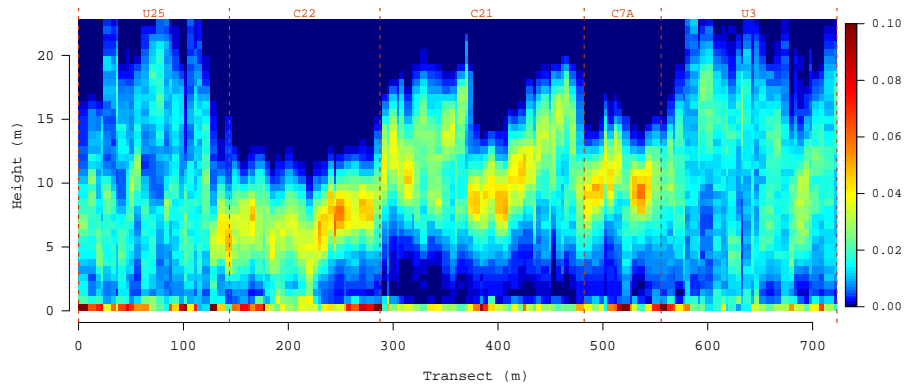
Parameter	Height knot models					
	$n_x^* = 2$	$n_x^* = 3$	$n_x^* = 4$	$n_x^* = 5$	$n_x^* = 6$	$n_x^* = 7$
RMSPE for AGB & LiDAR	0.887	0.859	0.826	0.8	0.797	0.793
CRPS for AGB & LiDAR	1955.91	1910.43	1833.09	1776.21	1767.83	1757.67
GRS for AGB & LiDAR	-1234.03	-1289.35	-1171.55	-1237.36	-1239.89	-1322.01
95% prediction coverage for AGB & LiDAR	93.9	93.5	92.7	91.5	91.1	90.9
RMSPE for AGB	0.317	0.316	0.308	0.311	0.309	0.31
CRPS for AGB	19.86	19.77	19.36	19.49	19.36	19.37
GRS for AGB	143.19	145.11	150.07	147.28	149.98	150.29
95% prediction interval coverage for AGB	92	92	91.1	92	92	92.9
95% prediction interval width for AGB	1.07	1.1	1.07	1.06	1.07	1.08

Results for the set of models with $v(\mathbf{s})$ set to zero are presented in the supplemental web

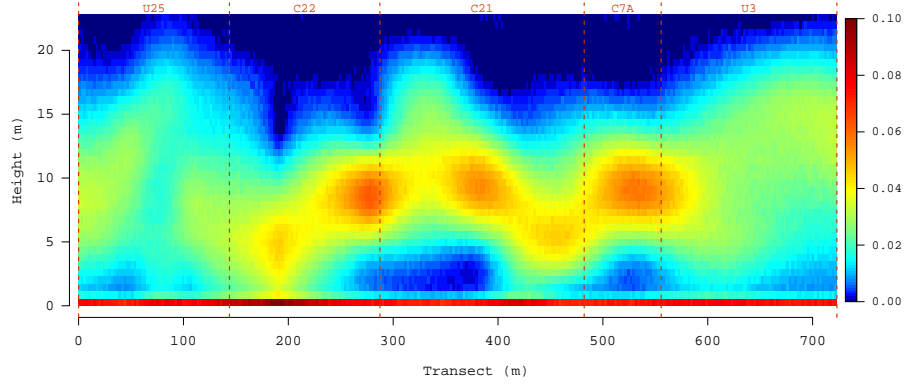
material. Here, fit and prediction is only influenced by the choice of n_x^* and n_u^* . Results show that inclusion of $v(\mathbf{s})$ has little effect on the *best* model selected using goodness-of-fit and out-of-sample prediction validation metric within each model set, i.e., n_u^* equal 339 and 170. This suggests that the underlying process seems to be driven by features shared between AGB and LiDAR and there is negligible information on features specific to AGB that are not shared by LiDAR. Hence, the shared AGB-LiDAR process. However, inclusion of $v(\mathbf{s})$ does marginally improve fit to the data and prediction. This improvement suggests there is some spatial structure in the residuals of AGB that is not captured by information from the LiDAR signals.

It is useful to consider a 2-dimensional slice through the data to further assess candidate model results. Figure 5(a) is the side-view of the observed LiDAR signals along the example transect denoted in Figure 3. Analogous to the portrayal in Figure 1(b), larger values of the signal correspond to greater density of tree material; hence, one could imagine Figure 5(a) is like looking at the side of a forest (15 m in width and \sim 700 m in length) where higher values correspond to denser forest and lower or zero values correspond to sparse or no forest. MU boundaries are also superimposed on Figure 5(a) and clearly show how different silvicultural treatments (i.e., tree harvesting) result in different vertical and horizontal distribution of tree material. For example, MU C22 is a young, short stature, forest versus the older, taller, and more vertically homogeneous forest in MU U3. As seen in Figure 3, no PSPs or knots in \mathcal{S}_u^* fall on the transect and hence the LiDAR signals in Figure 5(a) were not used for parameter estimation.

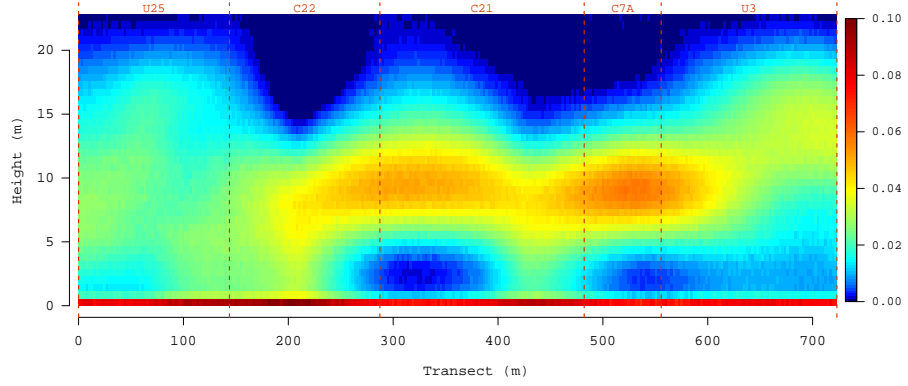
For brevity, we subsequently consider $n_x^* = 6$ candidate models but note that, in general, values of $n_x^* \geq 4$ yield comparable results. Signal prediction along the example transect using the $n_x^* = 6$ models are given in Figures 5(b) and 5(c). Comparison between these predictions and observed data, Figure 5(a), shows the candidate models capture the dominant trends in LiDAR signals. Reducing \mathbf{u}^* process knots by half, i.e., moving from the $n_u^* = 339$ to $n_u^* = 170$ model, does not greatly effect the vertical and horizontal distribution of predicted



(a) Observed LiDAR signal



(b) Predicted LiDAR signal with $n_u^* = 339$, $n_x^* = 6$



(c) Predicted LiDAR signal with $n_u^* = 170$, $n_x^* = 6$

Figure 5: Posterior predictive median for LiDAR signals along the example transect denoted in Figure 3.

signal values.

The observed signal data, Figure 5, suggests a strong space-height process interaction. The strength of this interaction is captured by γ in covariance function (2), where values close to one indicate strong interaction and values close to zero indicate weak interaction. Parameter estimates for γ in Tables 2 and 3 do indeed corroborate the presence of strong interaction between space and height. Figure 6 summarizes estimated space-height correlation and shows the median posterior correlation surface and associated contours using posterior samples from the $n_u^* = 170$ and $n_x^* = 6$ model. Here, at a given height the spatial correlation is small (i.e., 0.25) at ~ 0.5 km and negligible (i.e., 0.05) at ~ 1 km. This makes sense because the average areal extent of the MUs is a bit less than a half kilometer. Within a given signal, i.e., at a given spatial location, the correlation drops to 0.05 at ~ 4 m. Again, looking at Figures 1(b) and 5(a), we see fairly weak correlation in any given signal beyond several meters for most MUs.

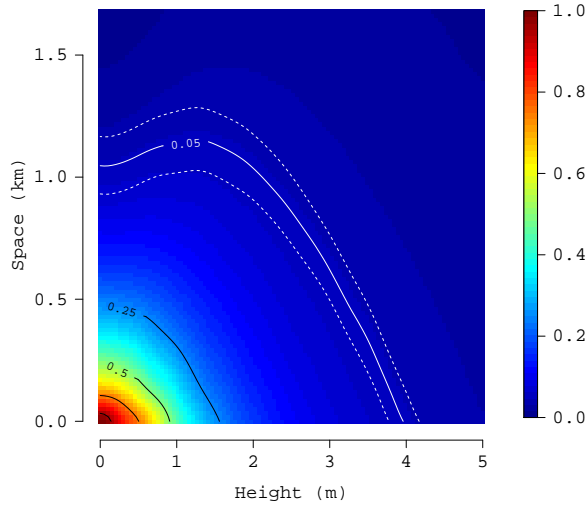
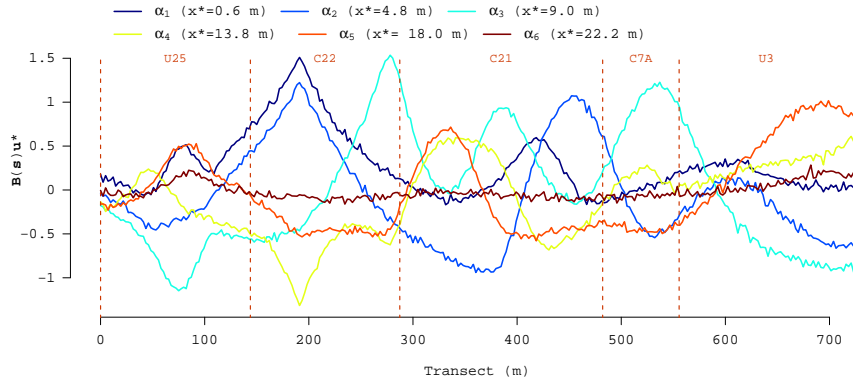


Figure 6: Space-height correlation posterior distribution median surface and contours. Median (solid white lines) and associated 95% credible interval (dotted white lines) for 0.05 correlation contour.

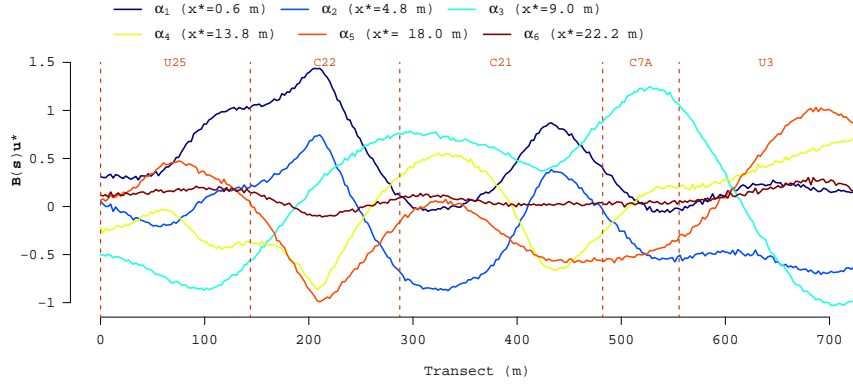
Figures 7(a) and 7(b) display the posterior median for each latent LiDAR regressor along

the example transect that correspond to the $n_x^* = 6$ model α estimates in Tables 2 and 3, respectively. Figure legends also include the x^* knot height associated with each latent regressor. The latent regressors interpretation becomes clear when Figure 5(a) is considered with Figures 7(a) or 7(b). For example, Figure 5(a) shows most of the forest material in MU C7A (between \sim 490-560 m along the example transect) is between \sim 5-12 m in height, hence we see large values of the latent regressor associated with $x^* = 9$ m and α_3 in Figures 7(a) and 7(b). Similarly, paucity of forest vegetation in the \sim 1-5 m height at \sim 300-370 m along the example transect, results in small values of the latent regressors associated with x^* equal to 0.6, and 4.8 m. Deviations seen between the latent regressor lines in Figures 7(a) and 7(b) and trends in Figure 5(a) are due to process smoothing that results from lack of PSPs and \mathcal{S}_u^* occurring on the example transect. This smoothing also accounts for difference seen between Figures 7(a) and 7(b).

Significant α parameter estimates suggest LiDAR signal trends captured by the low-rank models are useful for explaining variability in AGB. The impact of latent LiDAR regressors is seen in Figure 8 where both models capture AGB trends within MUs and along the example transect. Clearly spatial smoothing occurs—there should likely be more abrupt changes in median AGB across MUs—however with no predictors there is nothing to inform AGB predictions except for the smoothed representation of the LiDAR signals and residual spatial random effects. Other candidate models, including those presented in the supplemental web material, produce similar AGB profiles. We could certainly add a MU indicator or location specific predictors to help inform AGB prediction. However, these kind of data are rarely available in applied settings and a key objective of this analysis was to assess the usefulness of the latent LiDAR regressors for modeling AGB. Indeed, even lacking additional location specific predictor variables the candidate models yield very useful AGB data products that are critical inputs to forest management and MRV systems. For example, Figure 9 offers candidate models' AGB posterior predictive distribution median and associated measure of uncertainty at a 15×15 meter resolution for the entire PEF. This figure shows the candi-



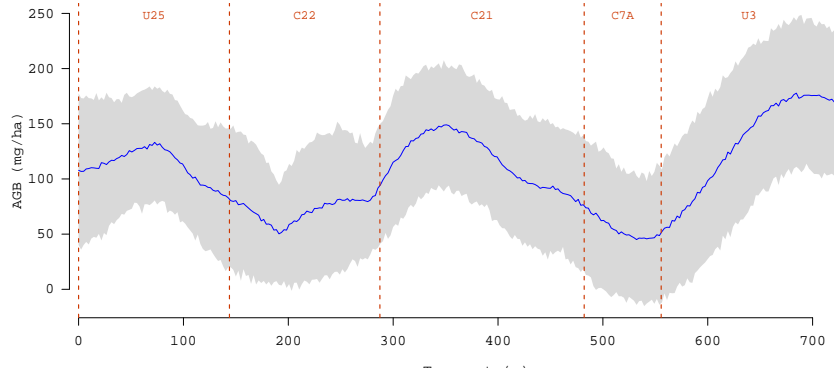
(a) Predicted latent LiDAR process with $n_u^* = 339$, $n_x^* = 6$



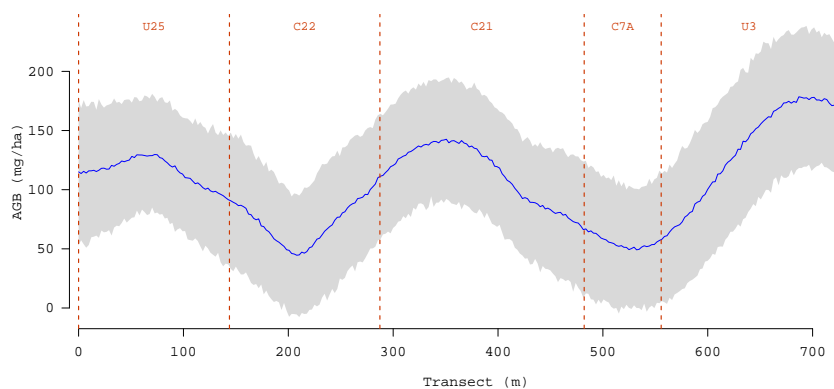
(b) Predicted latent LiDAR process with $n_u^* = 170$, $n_x^* = 6$

Figure 7: Posterior predicted distribution median of latent LiDAR signal regressors along the example transect denoted in Figure 3. The legend relates each regressor to the corresponding element in α with the predictive process knot height in meters is given in parentheses.

date models deliver nearly identical AGB prediction and uncertainty maps despite the large reduction in space-height process dimension. As expected, more precise AGB prediction occurs in proximity to observed PSP as shown by narrow 95% CI intervals in Figures 9(b) and 9(d).

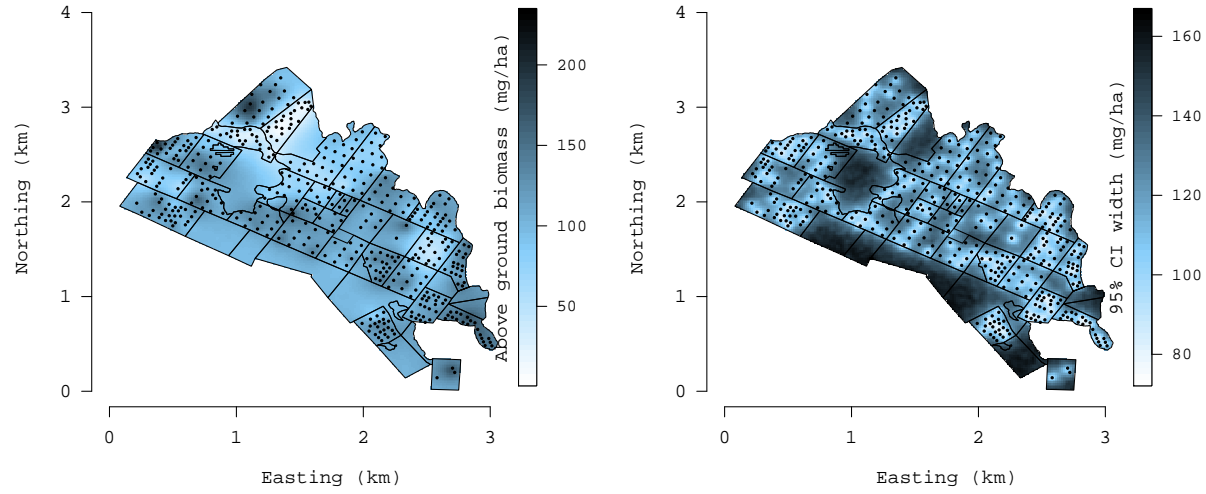


(a) Predicted AGB with $n_u^* = 339$, $n_x^* = 6$



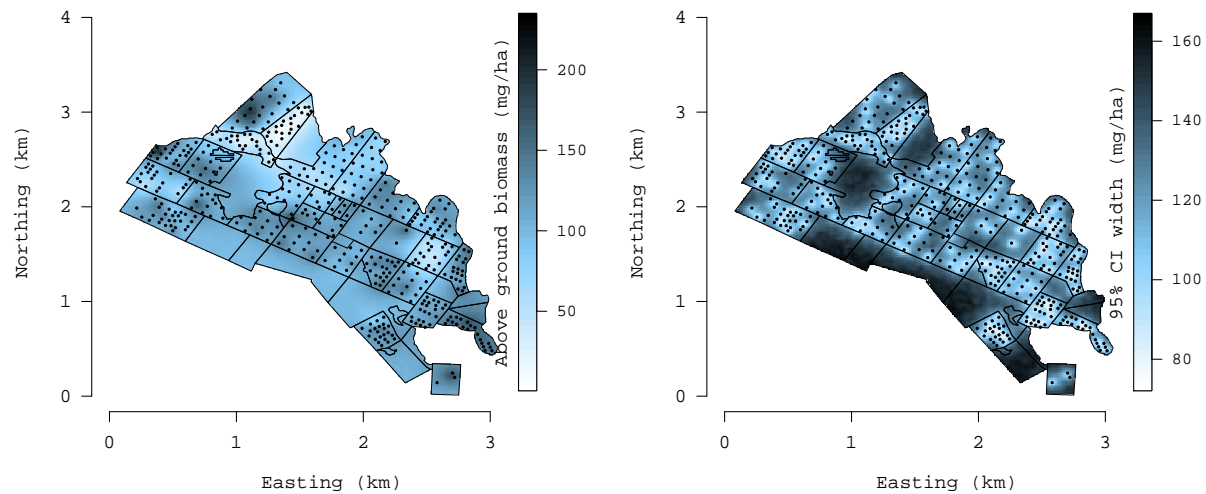
(b) Predicted AGB with $n_u^* = 170$, $n_x^* = 6$

Figure 8: Posterior predicted distribution median for AGB along the example transect denoted in Figure 3. MU identifiers are provided across the top of each panel.



(a) Predicted AGB with $n_u^* = 339, n_x^* = 6$

(b) 95% prediction interval width for AGB with $n_u^* = 339, n_x^* = 6$



(c) Predicted AGB with $n_u^* = 170, n_x^* = 6$

(d) 95% prediction interval width for AGB with $n_u^* = 170, n_x^* = 6$

Figure 9: Posterior predicted distribution's median and width of 95% prediction interval for AGB.

6 Summary

We have developed and implemented a class of Bayesian hierarchical models to jointly model LiDAR signals and AGB and effectively exploit the information from the high-dimensional LiDAR signals to explain AGB variability. We account for spatial dependence among and within the high-dimensional LiDAR signals and predict the LiDAR signals and AGB at arbitrary spatial locations and heights. We circumvent computational bottlenecks presented by the LiDAR signal dimensionality and number of spatial locations by applying reduced-rank predictive processes, a collapsed MCMC framework, and some efficient numerical linear algebra.

We opted for a fully process-based approach using covariance functions to exploit the easy constructibility and interpretability of the joint models. Alternative approaches could build upon existing functional data models that treat the high-dimensional signals as a function of space and height. For instance, one could possibly adapt the approach of Yang et al. (2015), who mapped agricultural soil properties, to build joint AGB-LiDAR models. Properties of these models and, in particular, their scalability to massive datasets still need to be explored.

Substantive contributions from the current PEF analysis include LiDAR-based maps of AGB with associated uncertainty that can inform analyses of MU specific silvicultural experiments and also serve as baseline estimates, with uncertainty, for future management and experiments. More broadly, we believe this modeling framework will be employed for future explorations and analysis relating LiDAR and similar high-dimensional signal data—generated by the missions detailed in Section 1—with AGB and other forest variables of interest. Future methodological extensions include analyzing several forest variables (e.g., AGB by tree species or structural variables such as density and basal area) perhaps correlated among themselves, as well as accounting for spatiotemporal associations. There is also considerable interest in adapting the proposed framework to model non-Gaussian forest variables such as forest/non-forest, fire risk categories, and species or functional types. We plan to extend this joint modeling framework to accommodate additional sparsely sam-

pled high-dimensional signal data such as hyper-spectral data that is similar to LiDAR but records information across the electromagnetic spectrum and can provide information on forest species or tree health status.

Future analysis of LiDAR and forestry data will need to cope with massive amounts of data and increasing demands on model scalability. Here, we could considerably enhance the scalability of the predictive process using the multi-resolution extensions in Katzfuss (2016), where we construct a sequence of nested predictive processes over a nested partition of the spatial domain. Alternatively, recent developments in massively scalable sparsity-inducing Nearest-Neighbor Gaussian Processes or NNGPs Datta et al. (2016) can be exploited. Our framework seamlessly accommodates such processes—we replace $u(\ell)$ and $v(\mathbf{s})$ in (5) with their NNGP counterparts instead of predictive processes. Rather than dimension reduction, scalability will be achieved exploiting sparsity structures in the resulting precision matrices. These models will be further explored and will be offered as a part of scalable Gaussian process models in the `spBayes` software package (Finley et al. 2015).

References

Abdalati, W., Zwally, H., Bindschadler, R., Csatho, B., Farrell, S., Fricker, H., Harding, Dand Kwok, R., Lefsky, M., Markus, T., Marshak, A., Neumann, T., Palm, S., Schutz, B., Smith, B., Spinhirne, J., and Webb, C. (2010), “The ICESat-2 Laser Altimetry Mission,” *Proceedings of the IEEE*, 98, 735–751.

Albercht, A., Hanewinkel, M., and Bauhus, J. (2012), “How Does Silviculture Affect Storm Damage in Forests of South-Western Germany? Results from Empirical Modeling Based on Long-Term Observations,” *European Journal of Forest Resources*, 131, 229–247.

Anderson, J. E., Plourde, L. C., Martin, M. E., Braswell, B. H., Smith, M.-L., Dubayah, R. O., Hofton, M. A., and Blair, J. B. (2008), “Integrating Waveform Lidar With Hyperspectral Imagery for Inventory of a Northern Temperate Forest,” *Remote Sensing of Environment*, 112, 1856–1870.

Asner, G., Hughes, R., Varga, T., Knapp, D., and Kennedy-Bowdoin, T. (2009), “Environmental and Biotic Controls over Aboveground Biomass Throughout a Tropical Rain Forest,” *Ecosystems*, 12, 261–278.

Awadallah, A., Abbott, V., Wynne, R., and Nelson, R. (2013), “Estimating Forest Canopy Height and Biophysical Parameters using Photon-counting Laser Altimetry,” in *Proc. 13th International Conference on LiDAR Applications for Assessing Forest Ecosystems (Silvi-Laser 2013)*, pp. 129–136.

Babcock, C., Matney, J., Finley, A., Weiskittel, A., and Cook, B. (2013), “Multivariate Spatial Regression Models for Predicting Individual Tree Structure Variables Using LiDAR Data,” *IEEE Journal of Selected Topics in Applied Earth Observations and Remote Sensing*, 6, 6–14.

Banerjee, S., Gelfand, A. E., Finley, A. O., and Sang, H. (2008), “Gaussian Predictive Process Models for Large Spatial Data Sets,” *Journal of the Royal Statistical Society: Series B (Statistical Methodology)*, 70, 825–848.

Blair, J. and Hofton, M. (1999), “Modeling Laser Altimeter Return Waveforms Over Complex Vegetation Using High-Resolution Elevation Data,” *Geophysical Research Letters*, 26, 2509–2512.

CMS (2010), “NASA Carbon Monitoring System,” <http://carbon.nasa.gov>, accessed: 5-22-2014.

Cook, B., Corp, L., Nelson, R., Middleton, E., Morton, D., McCorkel, J., Masek, J., Ranson, K., Ly, V., and Montesano, P. (2013), “NASA Goddards LiDAR, Hyperspectral and Thermal (G-LiHT) Airborne Imager,” *Remote Sensing*, 5, 4045–4066.

Datta, A., Banerjee, S., Finley, A. O., and Gelfand, A. E. (2016), “Hierarchical Nearest-Neighbor Gaussian Process Models for Large Geostatistical Datasets,” *Journal of the American Statistical Association*, in press.

Finley, A., Banerjee, S., and MacFarlane, D. (2011), “A Hierarchical Model for Quantifying Forest Variables Over Large Heterogeneous Landscapes With Uncertain Forest Areas,” *Journal of the American Statistical Association*, 106, 31–48.

Finley, A. O., Banerjee, S., and Gelfand, A. E. (2015), “spBayes for Large Univariate and Multivariate Point-Referenced Spatio-Temporal Data Models,” *Journal of Statistical Software*, 63.

Finley, A. O., Banerjee, S., Weiskittel, A. R., Babcock, C., and Cook, B. D. (2014), “Dynamic Spatial Regression Models for Space-Varying Forest Stand Tables,” *Environmetrics*, 25, 596–609.

GEDI (2014), “Global Ecosystem Dynamics Investigation LiDAR,” <http://science.nasa.gov/missions/gedi/>, accessed: 1-5-2015.

Gelfand, A. E. and Ghosh, S. K. (1998), “Model choice: A Minimum Posterior Predictive Loss Approach,” *Biometrika*, 85, 1–11.

Gelman, A., Carlin, J. B., Stern, H. S., Dunson, D. B., Vehtari, A., and Rubin, D. B. (2013), *Bayesian Data Analysis, 3rd Edition*, Chapman & Hall/CRC Texts in Statistical Science, Chapman & Hall/CRC.

Gneiting, T. (2002), “Nonseparable, Stationary Covariance Functions for Space-Time Data,” *Journal of the American Statistical Association*, 97(458), 590–600.

Gneiting, T., Genton, M. G., and Guttorp, P. (2006), “Geostatistical Space-Time models, Stationarity, Separability and Full Symmetry,” in *Statistical Methods for Spatio-Temporal Systems*, Chapman and Hall CRC Press, pp. 151–175, (eds Finkenstaedt, B. and Held, L. and Isham, V.).

Gneiting, T. and Guttorp, P. (2010), “Continuous-Parameter Spatio-Temporal Processes,”

Handbook of Spatial Statistics, 427–436, gelfand, A. E., Diggle, P., Fuentes, M. and Guttorp, P., editors, Chapman and Hall/CRC, pp. 427-436.

Gneiting, T. and Raftery, A. E. (2007), “Strictly Proper Scoring Rules, Prediction, and Estimation,” *Journal of the American Statistical Association*, 102, 359–378.

Gonzalez, P., Asner, G., Battles, J., Lefsky, M., Waring, K., and Palace, M. (2010), “Forest Carbon Densities and Uncertainties from LiDAR, Quickbird, and Field Measurements in California,” *Remote Sensing of Environment*, 114, 1561–1575.

Hayashi, R., Weiskittel, A., and Sader, S. (2014), “Assessing the Feasibility of Low-Density LiDAR for Stand Inventory Attribute Predictions in Complex and Managed Forests of Northern Maine, USA,” *Forests*, 5, 363–383.

Healey, S., Patterson, P., Saatchi, S., Lefsky, M., Lister, A., and Freeman, E. (2012), “A Sample Design for Globally Consistent Biomass Estimation Using Lidar Data from the Geoscience Laser Altimeter System (GLAS),” *Carbon Balance and Management*, 7, 10.

ICESat-2 (2015), “Ice, Cloud, and Land Elevation Satellite-2,” <http://icesat.gsfc.nasa.gov/>, accessed: 1-5-2015.

Iqbal, I., Dash, J., Ullah, S., and Ahmad, G. (2013), “A Novel Approach to Estimate Canopy Height Using ICESat/GLAS Data: A Case Study in the New Forest National Park, UK,” *International Jorunal of Applied Earth Observation and Geoinformation*, 23, 109–118.

Kampe, T., Johnson, B., Kuester, M., and Keller, M. (2010), “NEON: The First Continental-Scale Ecological Observatory with Airborne Remote Sensing of Vegetation Canopy Biochemistry and Structure,” *Journal of Applied Remote Sensing*, 4.

Katzfuss, M. (2016), “A Multi-Resolution Approximation for Massive Spatial Datasets,” *Journal of the American Statistical Association*, in press.

Le Toan, T., Quegan, S., Davidson, M., Balzter, H., Paillou, P., Papathanassiou, K., Plummer, S., Rocca, F., Saatchi, S., Shugart, H., et al. (2011), “The BIOMASS Mission: Mapping Global Forest Biomass to Better Understand the Terrestrial Carbon Cycle,” *Remote Sensing of Environment*, 115, 2850–2860.

Mateu, J. and Müller, W. (2012), *Spatio-Temporal Design: Advances in Efficient Data Acquisition*, John Wiley & Sons, Ltd.

Michener, W., Porter, J., Servilla, M., and Vanderbilt, K. (2011), “Long Term Ecological Research and Information Management,” *Ecological Informatics*, 6, 13–24.

Muss, J., Mladenoff, D., and Townsend, P. (2011), “A Pseudo-Waveform Technique to Assess Forest Structure Using Discrete Lidar Data,” *Remote Sensing of Environment*, 115, 824–835.

Næsset, E. (2011), “Estimating Above-Ground Biomass in Young Forests With Airborne Laser Scanning,” *International Journal of Remote Sensing*, 32, 473–501.

Neigh, C., Nelson, R., Ranson, K., Margolis, H., Montesano, P., Sun, G., Kharuk, V., Næsset, E., Wulder, M., and Andersen, H. (2013), “Taking Stock of Circumboreal Forest Carbon with Ground Measurements, Airborne and Spaceborne LiDAR,” *Remote Sensing of Environment*, 137, 274–287.

Ometto, J. P., Aguiar, A. P., Assis, T., Soler, L., Valle, P., Tejada, G., Lapola, D. M., and Meir, P. (2014), “Amazon Forest Biomass Density Maps: Tackling the Uncertainty in Carbon Emission estimates,” *Climatic Change*, 1–16.

Phillips, O. L., Malhi, Y., Higuchi, N., Laurance, W. F., Nez, P. V., Vsquez, R. M., Laurance, S. G., Ferreira, L. V., Stern, M., Brown, S., and Grace, J. (1998), “Changes in the Carbon Balance of Tropical Forests: Evidence from Long-Term Plots,” *Science*, 282, 439–442.

Popescu, S. and Zhao, K. (2008), “A Voxel-Based Lidar Method for Estimating Crown Base Height for Deciduous and Pine Trees,” *Remote Sensing of Environment*, 112, 767–781.

Sang, H. and Huang, J. Z. (2012), “A Full Scale Approximation of Covariance Functions for Large Spatial Data Sets,” *Journal of the Royal Statistical Society: Series B (Statistical Methodology)*, 74, 111–132.

Sendak, P. E., Brissette, J. C., and Frank, R. M. (2003), “Silviculture Affects Composition, Growth, and Yield in Mixed Northern Conifers: 40-year Results from the Penobscot Experimental Forest,” *Canadian Journal of Forest Research*, 33, 2116–2128.

Smith, W. (2002), “Forest Inventory and Analysis: A National Inventory and Monitoring Program,” *Environmental Pollution*, 116, Supplement 1, S233–S242.

Spiegelhalter, D. J., Best, N. G., Carlin, B. P., and van der Linde, A. (2002), “Bayesian Measures of Model Complexity and Fit,” *Journal of the Royal Statistical Society B*, 64, 583–639.

Stein, M. L. (2005), “Space-time Covariance Functions,” *Journal of the American Statistical Association*, 100, 310–321.

Stockton, N. (2014), “How a Flying Laser Built a 3-D Map of a Massive Alaskan Forest,” <http://www.wired.com/2014/12/alaska-laser-survey-3d-map>, accessed 2015-06-01.

Talbot, J., Lewis, S. L., Lopez-Gonzalez, G., Brien, R. J., Monteagudo, A., Baker, T. R., Feldpausch, T. R., Malhi, Y., Vanderwel, M., Murakami, A. A., Arroyo, L. P., Chao, K.-J., Erwin, T., van der Heijden, G., Keeling, H., Killeen, T., Neill, D., Vargas, P. N., Gutierrez, G. A. P., Pitman, N., Quesada, C. A., Silveira, M., Stropp, J., and Phillips, O. L. (2014), “Methods to Estimate Aboveground Wood Productivity from Long-Term Forest Inventory Plots,” *Forest Ecology and Management*, 320, 30–38.

Tonolli, S., Dalponte, M., Neteler, M., Rodeghiero, M., Vescovo, L., and Gianelle, D. (2011), “Fusion of Airborne LiDAR and Satellite Multispectral Data for the Estimation of Timber Volume in the Southern Alps,” *Remote Sensing of Environment*, 115, 2486–2498.

UN-REDD (2009), “The UN-REDD Programme,” <http://www.un-redd.org/>, accessed: 5-22-2014.

UNFCCC (2015), “United Nations Framework Convention on Climate Change,” <http://unfccc.int/2860.php>, accessed: 6-6-15.

West, P. (2004), *Tree and Forest Measurement*, Springer.

Wikle, C. K. (2010), “Low-Rank Representations for Spatial Processes,” *Handbook of Spatial Statistics*, 107–118, gelfand, A. E., Diggle, P., Fuentes, M. and Guttorp, P., editors, Chapman and Hall/CRC, pp. 107-118.

Xia, G., Miranda, M. L., and Gelfand, A. E. (2006), “Approximately Optimal Spatial Design Approaches for Environmental Health Data,” *Environmetrics*, 17, 363–385.

Yang, W.-H., Kikle, K. K., Holan, S. H., Myers, D. B., and Sudduth, K. A. (2015), “Bayesian Analysis of Spatially-Dependent Multi-Dimensional Functional Predictors,” *Statistica Sinica*, 25, 205–223.

Yeniay, O. and Goktas, A. (2002), “A Comparison of Partial Least Squares Regression with Other Prediction Methods,” *Hacettepe Journal of Mathematics and Statistics*, 31, 99–111.